Journal of Science: Advanced Materials and Devices 10 (2025) 101012

Contents lists available at ScienceDirect

Journal of Science: Advanced Materials and Devices

journal homepage: www.elsevier.com/locate/jsamd

Research Article

Layer-by-layer assembled hyaluronic acid/chitosan-coated Fe_3O_4@rGO nanoparticles: Synthesis and characterization for doxorubicin delivery in breast cancer cells

Aysa Azmoudeh [a,b,*], Seyma Sari [c], Miray Türk [e], Sencer Moral [a,d], Özen Kaya [f], Muhammet U. Kahveci [g], Gizem Dinler Doganay [e,h], Murat Kuşcu [b], Nesrin Erkol (Özören)[f], Duygu Ağaoğulları [a,**]

[a] Istanbul Technical University, Faculty of Chemical and Metallurgical Engineering, Department of Metallurgical and Materials Engineering, Particulate Materials Laboratories (PML), Graphene and 2D Materials Laboratory, Maslak, Istanbul, 34469, Türkiye
[b] Koç University, Department of Biomedical Science, Rumelifeneri Yolu, Sarıyer, Istanbul, 34450, Türkiye
[c] Istanbul Technical University, Graduate School, Chemistry Programme, Maslak, Istanbul, 34469, Türkiye
[d] Matil Materials Testing and Innovation Lab. Inc., Graphene and Nanomaterials Laboratory, Sarıyer, Istanbul, 34450, Türkiye
[e] Istanbul Technical University, Graduate School, Molecular Biology-Genetics and Biotechnology Department, Maslak, Istanbul, 34469, Türkiye
[f] Department of Molecular Biology and Genetics, Bogazici University, Bebek, Istanbul, 34342, Türkiye
[g] Istanbul Technical University, Faculty of Science and Letters, Department of Chemistry, Maslak, Istanbul, 34469, Türkiye
[h] Istanbul Technical University, Faculty of Science and Letters, Molecular Biology and Genetics Department, Maslak, Istanbul, 34469, Türkiye

ARTICLE INFO

Keywords:
Magnetic nanoparticles (MNPs)
Reduced graphene oxide (rGO)
Chitosan
Hyaluronic acid
Functionalization
Magnetic properties
Cytotoxicity

ABSTRACT

Magnetic nanoparticles (MNPs) are of significant interest for biomedical applications. Among them, Fe_3O_4 nanoparticles are widely used. However, they suffer from oxidation and reduced magnetization under physiological conditions. To overcome this limitation, Fe_3O_4@rGO (FR) nanoparticles were synthesized via a solvothermal method and optimized for 20 h reaction time. For further functionalization, the MNPs were coated with a multilayered polymeric shell consisting of alternating hyaluronic acid (HA) and chitosan (CHI) layers through a Layer-by-Layer (LbL) assembly method, with doxorubicin (DOX) embedded directly within the HA layers for controlled release, and referred to as FR-HC@DOX. In this design, rGO enhances structural stability, HA provides CD44-mediated targeting ability, and CHI improves biocompatibility. The LbL technique allows for precise control of coating thickness and uniform layer deposition, enhancing drug-loading efficiency and ensuring controllable release profiles. The optimized FR-HC@DOX maintained sufficient magnetic response (M_s = 26.04 emu/g) after drug loading, which is substantially higher than most reported polymer-coated Fe_3O_4 systems that typically drop below 20 emu/g. These magnetic nanocarriers also exhibited strong pH sensitivity (~100 % release at pH 5.5 vs 13 % at pH 7.4) and showed potent anticancer activity in MCF-7 cells while remaining biocompatible in MCF-12A healthy control cells at concentrations up to 80 μg/mL. This study presents a new approach by combining rGO embedded/coated Fe_3O_4 with multilayer HA/CHI coatings, creating a magnetic nanocarrier that improves the stability of Fe_3O_4, is controllable, pH-responsive, and targeted drug release. These results position the system as a distinctive and effective nanoplatform for magnetically guided, tumor-targeted chemotherapy.

1. Introduction

Nanoparticles (NPs) have gained significant importance in science and technology due to their unique size-dependent physicochemical properties [1]. Their small size and high surface-area-to-volume ratio allow for enhanced reactivity, controllable functionalities, and precise

* Corresponding author. Istanbul Technical University, Faculty of Chemical and Metallurgical Engineering, Department of Metallurgical and Materials Engineering, Particulate Materials Laboratories (PML), Graphene and 2D Materials Laboratory, Maslak, Istanbul, 34469, Türkiye.
** Corresponding author.
E-mail addresses: aazmoudeh23@ku.edu.tr (A. Azmoudeh), bozkurtdu@itu.edu.tr (D. Ağaoğulları).

https://doi.org/10.1016/j.jsamd.2025.101012
Received 30 June 2025; Received in revised form 15 September 2025; Accepted 22 September 2025
Available online 23 September 2025
2468-2179/© 2025 Vietnam National University, Hanoi. Published by Elsevier B.V. This is an open access article under the CC BY-NC-ND license (http://creativecommons.org/licenses/by-nc-nd/4.0/).

interactions with biological systems [2]. These characteristics have made NPs essential in diverse fields such as electronics [3], catalysis [4], environmental science [5], and most notably biomedicine [6], where they are contributing to significant advancements in diagnostics and targeted therapies [7]. Among the various types of nanoparticles, magnetic nanoparticles (MNPs) are of particular interest due to their superparamagnetic behavior at the nanoscale [8]. This enables them to respond effectively to external magnetic fields without retaining residual magnetization, a feature that makes them especially suitable for safe and reversible biomedical applications [9]. MNPs can be synthesized using a range of techniques such as co-precipitation [10], solvothermal processes [11], thermal decomposition [12], and laser pyrolysis [13]. These methods allow precise control over particle size, shape, and structure [14,15]. To extend their versatility, MNPs can also be encapsulated within droplet-based systems, forming magnetic droplets water-in-oil (W/O) and oil-in-water (O/W) emulsions that combine the magnetic functionality of solid nanoparticles with the adaptability of fluid carriers [16]. This form enhances magnetic control and mobility, making them highly effective for precision drug delivery, on-demand therapeutic release, and real-time biosensing applications [17]. To further enhance their performance, surface coatings, particularly with polymers such as poly(ethylene glycol) (PEG), poly(lactic-*co*-glycolic acid) (PLGA), poly(vinyl alcohol) (PVA), and polyethyleneimine (PEI), have been widely employed to improve colloidal stability, biocompatibility, and targeted drug delivery efficiency [18,19]. There are various coating strategies, such as physical adsorption [20], covalent bonding [21], layer-by-layer (LbL) assembly [22], and *in situ* polymerization [23]. Among them, the LbL assembly method has emerged as a highly effective approach, offering better control over surface functionality and loading capacity compared to conventional techniques [24]. These polymeric layers not only improve colloidal stability and biocompatibility but also allow for the modular addition of targeting ligands or therapeutic agents [25].

Despite extensive progress in magnetic nanocarriers for cancer therapy, most reported systems still face a fundamental challenge as Karthika et al. [26] coated rGO/Fe_3O_4 with chitosan, improving anticancer drug (DOX) loading (~0.45 mg mL^{-1}) and pH regulated release (pH ~5.5, mimicking the tumor microenvironment) and a much slower release profile at physiological pH (7.4), suggesting selective tumor-site activity, yet lacking modular control over shell thickness and release kinetics. Similarly, Dash et al. [27] combined rGO–HA with DOX and IR780 for in-vivo chemo-photothermal therapy, showing CD44-mediated targeting, while HA improved biocompatibility and active targeting, the platform lacked structural stabilization from multilayered shells, limiting its stability, reproducibility, and precise optimization of drug-release kinetics [28]. This emphasizes the need for modular LbL approaches, such as the HA/CHI multilayer system, which combine tumor targeting, pH-responsive drug release, and enhanced colloidal stability within a single reinforced nanoplatform. Polysaccharide based assemblies extend control further as Zhao et al. [29] designed LbL shells from HA and hydroxyethyl-chitosan, achieving controllable pH-responsive release (pH ~5.5–6.0) compared to physiological pH (7.4), demonstrating potential for selective tumor therapy. Furthermore, the incorporation of HA provided receptor-mediated targeting via CD44 binding, while HA-CHI contributed to stability and biocompatibility. This design validated the versatility of LbL polysaccharide coatings for constructing stimuli-responsive nanocarriers. The system was based purely on polymer layers and lacked reinforcement from inorganic cores such as rGO or Fe_3O_4, which are critical for achieving structural robustness, magnetic guidance, and multifunctionality. Beyond Fe_3O_4 and GO platforms, multifunctional nanocomposites highlight similar challenges. Namazi et al. [30] integrated Cu-MOF, GO, Fe_3O_4, and hydroxyapatite into an L-lysine-modified carrier with excellent DOX encapsulation (~96.5 %) and controlled pH release, but successive modifications reduced M_s to ~18 emu·g^{-1} far lower than bare Fe_3O_4, thereby limiting the carrier's potential for magnetic guidance. Krishnaveni et al. [31] proposed a ROS/pH-responsive Fe_3O_4@saponin/PEI carrier with strong magnetization (~75 emu·g^{-1}) and 89 % DOX encapsulation but lacking receptor specific targeting.

In this study, Fe_3O_4@rGO (FR) nanoparticles were synthesized via solvothermal processing at reaction times of 10, 15, and 20 h and calcination at 500 °C for 1 h. To improve their dispersion in solution and to make them more biocompatible, the nanoparticles were coated through the LbL method. The rGO prevents Fe_3O_4 oxidation and enhances crystallinity and stability [11], HA enables tumor targeting through CD44 receptor binding [32], and CHI contributes biocompatibility and electrostatic stabilization [33]. DOX was incorporated into HA layers to allow pH-responsive release, with the multilayer design ensuring high drug loading capacity, controlled kinetics and forming FR-HC@DOX MNPs as a multifunctional nanocarrier that unites structural stability, magnetic guidance, selective targeting, and responsive release. To the best of our knowledge, this designed form of FR-HC@DOX MNPs has been used for the first time to investigate their potential in biomedical applications such as magnetically guided, pH-responsive drug delivery in cancer nanomedicine. Characterization confirmed successful coating and drug incorporation, with optimized FR-HC@DOX MNPs showing a sufficient magnetic response after DOX loading. *In vitro* drug release, cytotoxicity, and cellular uptake studies demonstrated that FR-HC@DOX exhibited strong pH sensitivity, dose-dependent anticancer activity, significantly reducing MCF-7 breast cancer cells' viability after 24 and 48 h of treatment. The cell-based studies, together with *in vitro* drug release experiments, suggest that the nanoparticles are internalized via HA receptor-mediated endocytosis.

2. Experimental

2.1. Materials and methods

Chitosan (Sigma-Aldrich, from shrimp shells, ≥75 % purity (deacetylated)), ferrocene ($FeC_{10}H_{10}$, ISOLAB, 99 % purity), hyaluronic acid (Sigma-Aldrich, ≥95 % purity, M_w: 500–800 kDa), sodium chloride (Merck, 99.5 % purity), graphene oxide (GO, AEROFEN), acetic acid (Merck, glacial, 100 % purity), potassium chloride (Merck, 99.5 % purity), potassium hydroxide (CHEMSOLUTE®-Th. Geyer, 99.5 % purity), di-sodium hydrogen phosphate dihydrate (Merck, 99.5 % purity, $Na_2HPO_4.H_2O$), potassium dihydrogen phosphate (Merck, 99 % purity, KH_2PO_4) were used as a raw powder material. Fetal bovine serum (FBS) (Gibco, 10500064), Penicillin-Streptomycin (Gibco, 15140122), dimethyl sulfoxide (DMSO) (GENAXXON, >99.5 % purity, cell culture grade, M6323.0100), and Thiazolyl Blue Tetrazolium Bromide (MTT) (BIOMATIK, A3338-250 MG) were used as liquid materials in the experiments.

2.2. Solvothermal synthesis of Fe_3O_4@rGO nanoparticles

To synthesize magnetic Fe_3O_4@rGO (FR) nanoparticles, ferrocene ($FeC_{10}H_{10}$) and graphene oxide (GO) powders were used as starting materials based on previous study [11]. In a typical process, 0.02 g of GO (0.67 mg/mL in 30 mL DI water) was dispersed by magnetic stirring 500 rpm for 15 min. 0.14 g ferrocene (~0.75 mmol) was dissolved in 30 mL of acetone and ultrasonicated for 20 min (bath sonicator, 40 kHz, 200 W) to ensure homogeneous dispersion. These two solutions were then mixed, followed by the addition of 0.1 mL hydrogen peroxide (30 % w/w, 8.8 M) as oxidant, and the mixture was stirred for another 45 min. The resulting solution was transferred into a 50 mL Teflon-lined stainless-steel autoclave (70–80 % fill volume) and heated at 200 ± 5 °C for 10, 15, and 20 h. After cooling naturally to room temperature, the product was collected by centrifugation at 1000 rpm for 10 min per cycle, repeated three times, and washed with acetone three times, and then the decanted residues were dried at 60 °C under vacuum overnight.

The calcination process was conducted under argon gas (Linde, 99.99 % purity) at 500 °C for 1 h to enhance crystallinity and magnetic behavior. Solvothermal synthesis of magnetic Fe_3O_4@rGO (FR) nanoparticles is represented schematically as step 1 in Fig. 1.

2.3. Coating of FR-HC@DOX

FR-HC@DOX was obtained by layer-by-layer HA/CHI coating of FR (20 h, after calcination) via electrostatic interaction motifs, with modified from previous studies [34,35], as illustrated in Step 2 of Fig. 1. The FR nanoparticles synthesized via the solvothermal method were immersed in the first polyelectrolyte solution (HA, 1 mg/mL in 0.14 M aqueous NaCl, 30 mL) containing DOX (0.6 mM) and mixed on a shaker for 15 min. The polyelectrolyte containing DOX solution was removed by centrifugation at 5000 rpm for 5 min, the nanoparticles were rinsed three times with 0.15 M NaCl solution followed by centrifugation at each step. The nanoparticles were immersed in the oppositely charged polyelectrolyte solution (CHI, 1.5 mg/mL in 0.1 M acetic acid (pH 4) containing 0.14 M NaCl, 30 mL) and mixed on a shaker for 15 min. The polyelectrolyte was removed by centrifugation at 5000 rpm for 5 min, followed by the same washing procedure. The LbL procedure was repeated two more times. Finally, the nanoparticles were immersed in a DOX-free HA solution (HA, 1 mg/mL in 0.14 M aqueous NaCl) and mixed on a shaker for 15 min, then, washed by removing the solution via centrifugation at 1000 rpm for 10 min per cycle, followed by three rinses with 0.15 M NaCl and two rinses with pure water. FR-HC@DOX MNPs were collected by centrifugation and dried using a lyophilizer for 2 days. The obtained nanoparticles were stored at +4 °C until further use. DOX-free FR-HC nanoparticles were also prepared using the same procedure without addition of DOX.

2.4. Evaluation of drug loading capacity and in vitro release of DOX from FR-HC@DOX

Drug loading capacity (DLC, %) was evaluated according to the previously reported approach [36], as given in Eq. (1). The lyophilizer-dried FR-HC@DOX (5 mg) was dispersed in 5 mL of DMSO, allowing DOX to be released completely from FR-HC@DOX. The DOX content of the FR-HC@DOX was determined using a UV–Vis spectrophotometer at 484 nm, based on a DOX calibration curve prepared in DMSO.

$$\text{DLC}\ (\%) = \frac{\text{mass of the drug encapsulated in FR-HC@DOX}}{\text{mass of FR-HC@DOX containing the drug}} \text{ x } 100\ (\%) \quad \text{Eq.(1)}$$

The *in vitro* release kinetics of DOX from FR-HC@DOX MNPs were evaluated using a shaker (DLAB MX-T6-S Analog Tube Shaker, 0–70 rpm, 6 cylinders) at room temperature. The dried FR-HC@DOX MNPs were weighed into amber vial. Phosphate buffered saline solutions (PBS) at pH 5.5 (mimicking the endosomal environment) or pH 7.4 (resembling physiological conditions) were added to achieve a final concentration of 1 mg/mL. The samples were placed on the shaker (DLAB MX-T6-S Analog Tube Shaker, 0–70 rpm, 6 cylinders) set to 35 rpm at room temperature and constantly shaken. FR-HC@DOX was withdrawn from the medium at predetermined time intervals over a period of two days using a magnet, and the absorbance of the release medium was measured. The amount of DOX released from FR-HC@DOX was determined by measuring absorbance at 484 nm using a UV–Vis spectrophotometer, based on a DOX calibration curve prepared in PBS at pH 7.4 or 5.5. The cumulative release of DOX was calculated by using Eq. (2) in the following equation:

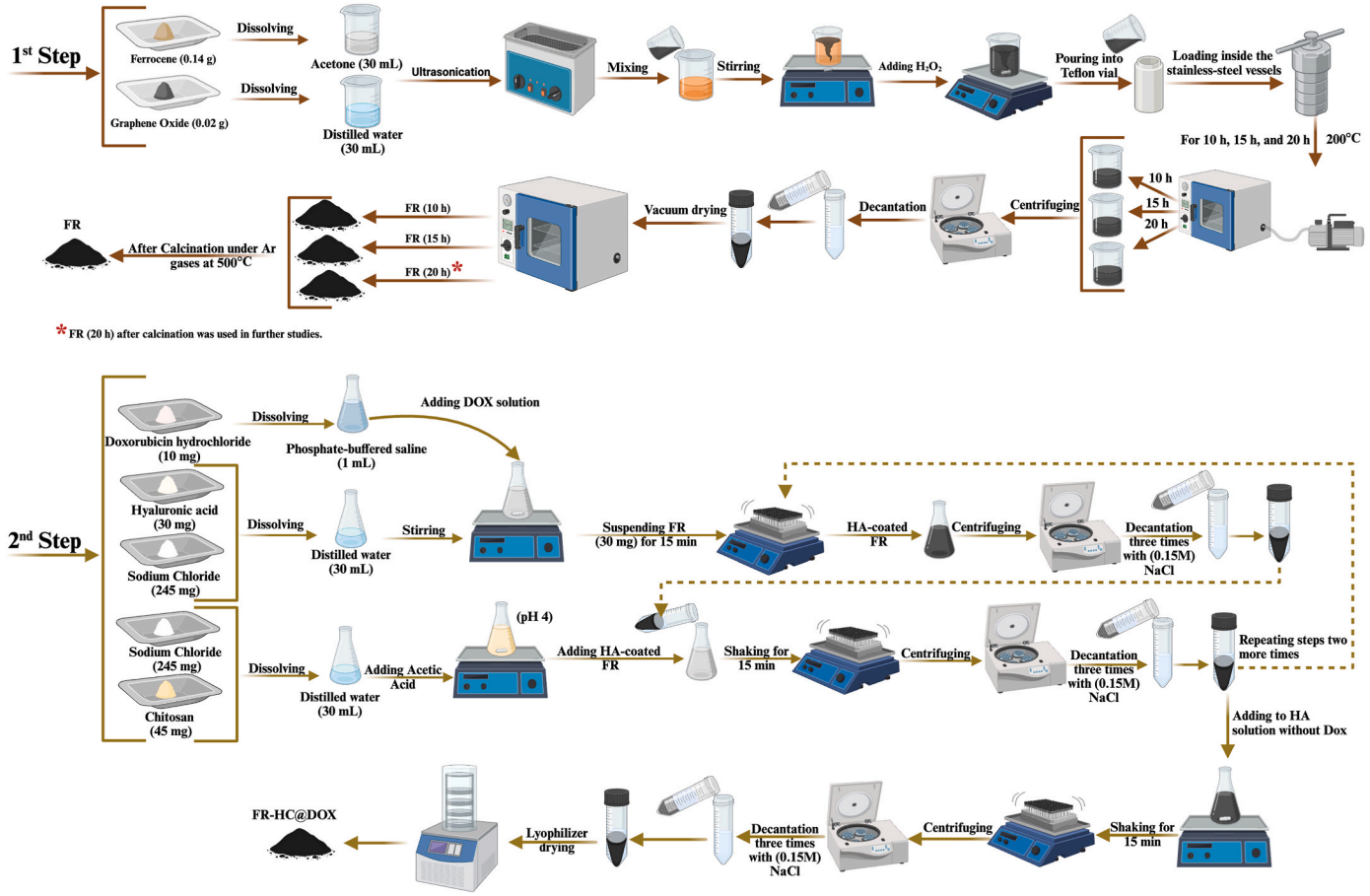


Fig. 1. Schematic of all utilized steps in synthesizing FR and FR-HC@DOX. (created using BioRender.com).

$$\text{Cumulative release } (\%) = \frac{\text{mass of DOX release at time of t}}{\text{total mass of DOX in FR-HC@DOX}} \text{ x } 100\% \quad \text{Eq. (2)}$$

2.5. Characterization of nanoparticle-induced cytotoxicity and cellular uptake

MCF-7 breast cancer (HTB-22, ATCC) and MCF-12A non-tumorigenic healthy control breast epithelial cells (CRL-3598, ATCC) were cultured as recommended by the manufacturer. MCF-7 cells were maintained in high-glucose DMEM medium (Gibco, 41966029) supplemented with 10 % FBS and 1 % penicillin-streptomycin under standard culture conditions at 37 °C in a humidified air containing 5 % CO_2. MCF-12A cells were cultured in a 1:1 mixture of DMEM and Ham's F12 medium (Gibco, 11320033) supplemented with 20 ng/mL Human epidermal growth factor (EGF, Gibco, PHG0311), 100 ng/mL cholera toxin (Sigma, C8052), 0.01 mg/mL bovine insulin (Capricorn Sci, INS-K), 500 ng/mL hydrocortisone (Sigma, H0888), 5 % horse serum (Gibco, 26050088) and 1 % penicillin-streptomycin. Upon reaching 80–90 % confluency, cells were detached by trypsinization (Gibco, 25200056) and seeded into 96-well plates at a density of 5×10^3 cells per well in 100 µl of complete medium, followed by incubation overnight under standard conditions to allow cell attachment and growth. Nanoparticle sample stocks were prepared at a concentration of 40 mg/mL in cell culture grade DMSO and gently mixed overnight. These stock solutions were diluted to the desired concentrations using serial dilution in cell culture grade DMSO. Cells were subjected to nanoparticle treatment at a final concentration from 2×10^{-2} µg/mL to 8×10^1 µg/mL. Given that DMSO served as the solvent, negative controls were treated with matching DMSO volumes, with its final concentration uniformly maintained at 2 % across all conditions, as determined to be the upper limit of cellular tolerance. Each condition was performed as triple technical replicates. To account for potential precipitation that could interfere with spectroscopic measurements, a no-cell control was included for each dosage. The average absorbance of each no-cell condition was subtracted from the corresponding cell-treatment condition. Relative cell viability was calculated in comparison to the DMSO control. Cytotoxicity was assessed after 6, 24 or 48 h of incubation. 10 µL MTT solution (5 mg/mL in PBS) was added during the final 3 h of each incubation period. The medium was removed upon completion of the incubation and formazan crystals were dissolved in 100 µL DMSO. Absorbance was measured at 570 nm, with background correction at 630 nm, using a microplate spectrophotometer (Benchmark Plus Microplate Reader, Bio-Rad). Relative cell viability was calculated according to the DMSO control of each set. Experiments were conducted with two biological and three technical replicates. Statistical analysis and graph preparation were performed using GraphPad Prism 8.01. Statistical significance was determined using unpaired one-tailed Student's t-test. $P \leq 0.05$ (*), $P \leq 0.01$ (**), or $P \leq 0.001$ (***).

For immunocytochemistry experiments, MCF-7 cells were seeded as 3×10^5 cell per well in 12-well plate containing gelatin (Sigma Aldrich, G1393) coated coverslips. Next day, cells were treated with nanoparticles at 40 µg/ml final concentration. 24 h post-transfection, medium was removed, and cells were washed three times with PBS to remove residual extracellular nanoparticles. Upon cell fixation with pre-chilled 4 % paraformaldehyde (Sigma-Aldrich, P6148) for 10 min at room temperature, cells were blocked with blocking solution (3 % BSA, 0.1 % Triton X-100 in PBS) for 1 h at room temperature. Following thorough washing, coverslips were mounted on glass slides in ProLong Diamond Antifade mounting medium containing DAPI (Thermo Fisher, P36962). All confocal images were obtained using ×40 objective via Zeiss, Axio Observer Z1 confocal microscope. For DOX detection, samples were excited at 488 nm and emission spectra were collected between 524 and 770 nm.

For flow cytometry analysis, MCF-12A cells were grown as described. Upon reaching 90 % confluency, cells were collected via trypsinizaton, then, 4×10^5 cells were seeded to each well of 6-well plates. Upon reaching 80 % confluency, cells were treated with FR-HC or FR-HC@DOX MNPs at 40 µg/ml final concentration. Upon 24 h treatment, media was discarded, and cells were washed with PBS 3 times to remove residual nanoparticles. Also, non-internalized present nanoparticles were also removed by additional PBS wash steps using magnetic field.

Apoptotic cells were quantified by Annexin V–FITC staining and flow cytometry. Cells were cultured as described. Cells were collected upon reaching 90 % confluency, then, collected by trypsinization. 1×10^6 cells were seeded to each well of 6-well plate. Next day, cells were treated with FR-HC or FR-HC@DOX MNPs at 40 µg/ml final concentration for 24 h. Upon incubation, cells were harvested by trypsinization, washed three times with PBS, and resuspended in Annexin V binding buffer (BD Pharmingen™ FITC Annexin V Apoptosis Detection Kit I). Cells (1×10^5 in 100 µL) were incubated with Annexin V–FITC (5 µL) for 15 min at room temperature in the dark, diluted with 400 µL binding buffer, and analyzed within 1 h on a BD FACSCalibur. Samples were acquired on a 488 nm cytometer with FITC in FL-1 (~530/30 nm) and doxorubicin autofluorescence in FL-2 (~585/42 nm). Cells were gated by FSC-H/SSC-H, and Annexin V positivity thresholds were defined using unstained controls. 10,000 events were recorded per sample.

2.6. Characterization investigations

The phases of the synthesized powders were examined using X-ray diffraction (XRD, Bruker Advanced Series) with a CuK_α radiation source. The measurements were done at 35 kV and 40 mA, using a wavelength of 1.54060 Å. The scan speed was 2° per minute, covering a 2θ range from 20° to 70° in 0.02° steps. Raman spectroscopy was used at room temperature to study the structural features of the magnetic nanoparticles, using a Renishaw Invia Raman Microscope with a 532 nm laser. The surface elements (iron, carbon, and oxygen) were analyzed using X-ray photoelectron spectroscopy (XPS, Thermo K-Alpha system). Magnetic properties were tested at room temperature using a vibrating sample magnetometer (VSM, Lake Shore 7407), with measurements taken under a magnetic field up to 10,000 Oe using a non-magnetic holder. The shape and structure of FR and FR-HC@DOX MNPs were visualized using high-resolution transmission electron microscopy (TEM, HT7800, 120 kV), along with elemental mapping using EDX. Zeta potential was measured with a Malvern Mastersizer 2000 to determine the surface charge and stability of the nanoparticles in liquid. The chemical bonds and functional groups were analyzed using Fourier-transform infrared spectroscopy (FTIR, Bruker Alpha-T) in the range of 4000–400 cm^{-1} using an ATR accessory at room temperature. Drug loading and release evaluations were performed using a Peak Instruments C-7000UV UV–Vis spectrophotometer equipped with a 1 cm path length cuvette. Absorbance measurement for cell viability was performed at 570 nm by microplate spectrophotometer (BIO-RAD Benchmark Plus) for all magnetic nanoparticles after calcination process. DOX loading was checked by a fluorescence spectrometric approach. For this analysis, 200 µL of each nanoparticle stock solution (0.4 mg/mL) prepared in DMSO was dispensed into individual wells of a black 96-well microplate (Corning, 3991). Fluorescence measurement conditions were determined according to the fluorescence properties of DOX [37]. Three technical replicates were used, and DMSO-only control was used as negative control. Samples were excited at 470 nm with 10 nm bandwidth and emission spectra were collected by scanning the fluorescence signal from 520 nm to 700 nm with 10 nm bandwidth and 1 nm stepwidth by CLARIOstar Plus microplate reader (BMG Labtech). Fluorescence spectra were plotted using GraphPad Prism 8.01. Confocal images were taken using ×40 objective via Zeiss, Axio Observer Z1 confocal microscope.

3. Results and discussion

3.1. XRD, DLS, Raman, XPS, and FT-IR characterization of the samples

For the phase determination and structural evaluation of FR nanoparticles synthesized via a solvothermal process at 10, 15, and 20 h, X-ray diffraction (XRD) analysis was conducted both before and after calcination as shown in Fig. 2a and b. The goal was to evaluate the crystalline behavior of Fe_3O_4 and to observe the reduction of GO to rGO. Before calcination process in all three samples (10 h, 15 h, and 20 h), the characteristic diffraction peaks at 2θ values of approximately 30.1°, 35.5°, 37.1°, 43.2°, 53.5°, 57.1°, and 62.7° correspond well to the (220), (311), (222), (400), (422), (511), and (440) planes of Fe_3O_4 (JCPDS No. 19–0629), confirming the formation of magnetite in a cubic spinel structure [38]. After calcination, the intensity and sharpness of this peak increase significantly, indicating improved crystallinity and grain growth, which enhances the structural ordering of the magnetic phase [11,39]. Additionally, a broad and low-intensity peak around 24–26° is observed in all samples, which is attributed to the (002) plane of GO [40]. This broad feature indicates the presence of disordered and stacked GO layers with oxygen-containing functional groups. Among the samples, the 20 h synthesis time leads to sharper and stronger Fe_3O_4 peaks, suggesting improved crystallinity and particle growth over extended reaction duration. Meanwhile, the GO-related peak becomes slightly sharper from 10 to 20 h, implying gradual reduction of GO and restoration of sp^2-carbon domains. Also, after calcination, the XRD patterns still exhibit prominent Fe_3O_4 peaks at the same positions, indicating thermal stability of the magnetic phase. A significant change is noted in the carbon-related peaks. The broad (002) peak of GO that was evident before calcination becomes narrower and shifts slightly, appearing as a clearer peak near 26.4°, which corresponds to graphitic carbon C rather than GO. This shift suggests that calcination effectively reduces GO to rGO, eliminating oxygen groups and promoting partial graphitization [11,40]. This behavior is more noticeable in the 20 h sample, consistent with its already partially reduced state prior to calcination. Indrayana et al. [39], reported that by increasing calcination time/temperature improved lattice ordering in Fe_3O_4 and increased crystallinity by ~10 %. Compared with Sarikhani et al. [41], observed broader Fe_3O_4 peaks in cystamine-crosslinked Fe_3O_4@GO due to structural disorder, the FR nanoparticles retain sharper and more intense reflections, suggesting that the rGO matrix stabilizes the crystalline magnetite phase even after surface functionalization, so enhanced crystallinity is functionally important because it supports stronger magnetic ordering, which is essential for reliable external field guidance.

The particle size distribution obtained from DLS measurements are shown in Fig. 2c–e. Average particle size for the FR (10 h, 15 h, 20 h) samples after calcination are approximately 68 nm for 10 h, 141 nm for 15 h, and 164 nm for 20 h. All samples exhibit narrow, indicating uniformity in particle size and good colloidal stability [11,42]. The gradual increase in particle size with longer reaction times can be attributed to enhanced crystal growth and further agglomeration around the rGO

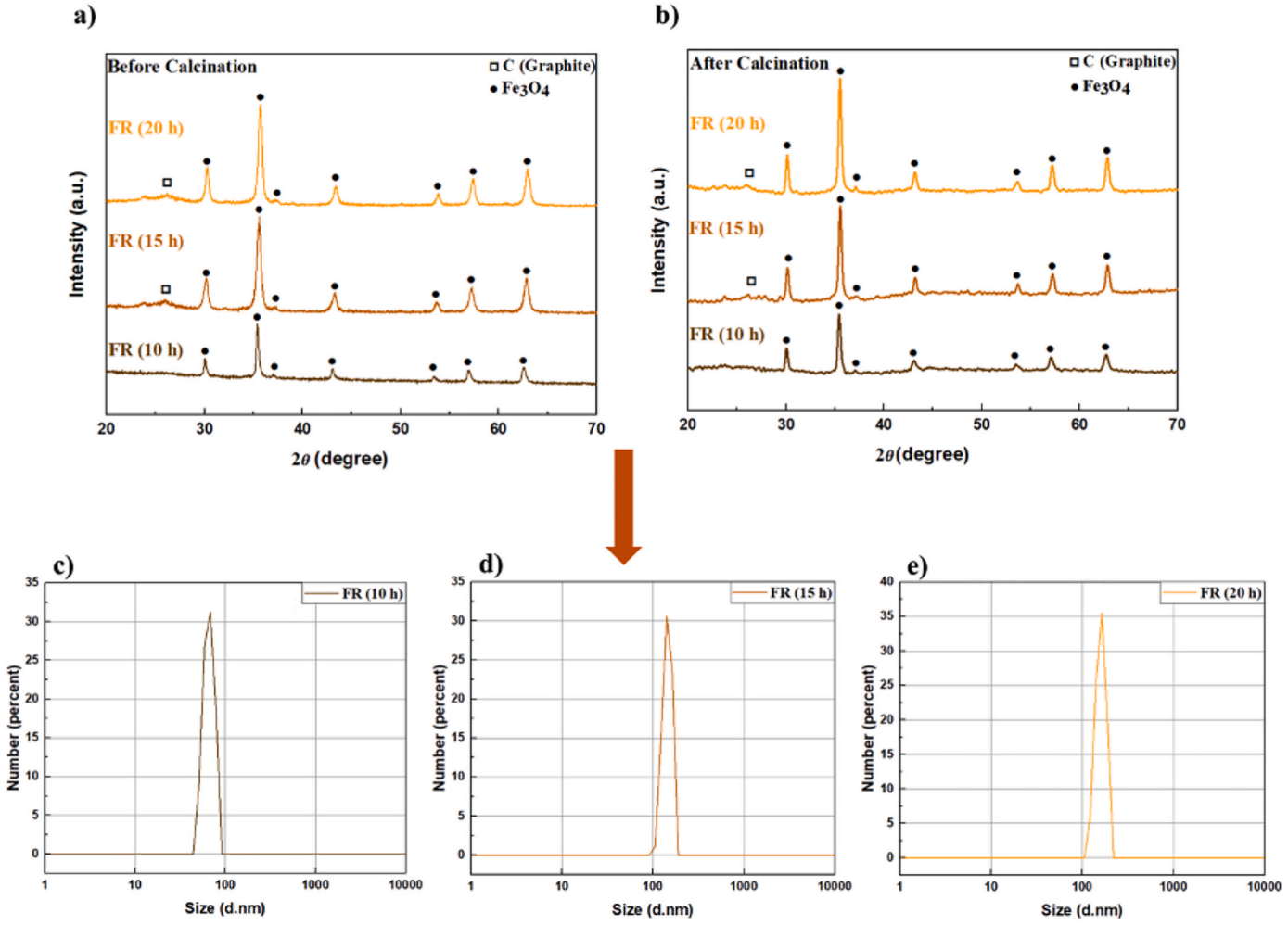


Fig. 2. (a) XRD patterns of FR magnetic nanoparticles synthesized at 10 h, 15 h, and 20 h before calcination, and (b) those after calcination. (c–e) DLS particle size distributions of FR (10 h), FR (15 h), and FR (20 h) samples.

sheets during synthesis.

Raman spectroscopy was employed to characterize the crystal structure evolution of solvothermally synthesized FR nanoparticles at various stages, including different synthesis durations, post-calcination, and surface functionalization via the LbL polymer coating method, both in the presence and absence of the anticancer drug DOX, as shown in Fig. 3.

All spectra exhibit the characteristic Fe_3O_4 bonds at the Raman shifts of 208.55, 273.30, and 388.20 cm^{-1}, also D (~1350 cm^{-1}) and G (~1580 cm^{-1}) bands of graphitic carbon [11,43]. The D band reflects disorder and defects in the sp^2 carbon lattice, while the G band corresponds to plane vibrations of graphitic domains [44]. The G′ or 2D (2700–2715 cm^{-1}) band is second order overtone of the D band and arises from a two-phonon, double-resonance scattering process in sp^2 carbon systems. The D + G (2900–2950 cm^{-1}) bond is combination mode that arises from the simultaneous excitation of both the D and G phonons [45]. Unlike the 2D band, which is a second-order signal related to the D band, the D + G band is not a higher-order feature but a combination mode that arises from the simultaneous vibration of both D and G phonons [11,44]. Its appearance mostly in reduced graphene oxide (rGO), amorphous carbon, and multi-layer defective graphene [45]. In the initial samples synthesized at 10, 15, and 20 h, the G′ (2D) band becomes more prominent with increasing synthesis time, indicating a higher degree of GO reduction to rGO, so solvothermal treatment enhancing the removal of oxygen-containing groups and restoring sp^2 domains. Among these, the 20 h sample shows the most noticeable 2D signal, suggesting improved graphitic structure. Also, the intensity of the Fe_3O_4 peaks slightly increases with longer synthesis times from 10 h to 20 h, suggesting improved crystallinity and stronger interactions between Fe_3O_4 and rGO.

The I_D/I_G intensity ratios 0.88, 0.87, and 0.86 for the 10, 15, and 20 h samples support this improvement. After calcination, a clear shift occurs at the I_D/I_G ratio increases to 1.10, indicating a rise in defects, likely due to thermal damage or oxidation, the 2D band remains strong, suggesting that despite structural defects, some graphitic order is retained or even stacked multilayers form due to thermal reorganization [44,45]. The LbL coating decreased the I_D/I_G ratio to 0.78, suggesting that the polymer layers passivated surface defects or partially reorganized the carbon structure. This is functionally significant, as HA/CHI passivation likely improves colloidal stability and reduces uncontrolled drug adsorption, while preserving π–π sites for controlled DOX loading. After DOX incorporation, the I_D/I_G ratio increased to 0.86, consistent with π–π stacking between DOX aromatic rings and rGO. This behavior matches reports on DOX with graphene carriers as Huang et al. [46] showed by SERS that π–π stacking drives DOX loading on GO, while acidic conditions trigger release; Balcioglu et al. [47] demonstrated ultra-high loading (6.05 mg mg^{-1}) in GO–Fe_3O_4–AuNP, with Raman confirming dominant DOX–graphene interactions. Such systems highlight how π–π stacking, while efficient for loading, increases Raman defect signatures. Importantly, unlike Fe_3O_4–rGO aerogels studied by Scheibe et al. [48], where I_D/I_G rose from ~0.9 to ~1.05 after nanoparticle anchoring, the LbL HA/CHI coating reduced I_D/I_G to 0.78, showing superior defect passivation while still preserving π–π sites for DOX. This platform uniquely combines defect control, stable drug loading, and pH-responsive release.

X-ray photoelectron spectroscopy (XPS) was conducted to investigate the surface chemical composition and bonding states of the synthesized samples at various stages of functionalization. Fig. 4a presents the wide scan and high-resolution spectra for FR (20 h), after calcination of FR (20 h), FR-HC, and FR-HC@DOX and detailed plots of FR synthesized for 10 h and 15 h are shown in Fig. S1 [49]. In the survey spectra Fig. 4a–d, all samples show characteristic peaks of Fe 2p, O 1s, and C 1s, indicating the presence of iron oxide, oxygen functionalities, and carbon materials [50]. In Fig. 4c and d, additional peaks for N 1s emerge, confirming the successful introduction of nitrogen containing biomolecules such as chitosan and DOX. The growing N 1s intensity from c to d reflects the successive addition of these functionalities. High resolution Fe 2p spectra a_1–d_1 further confirm the oxidation state of

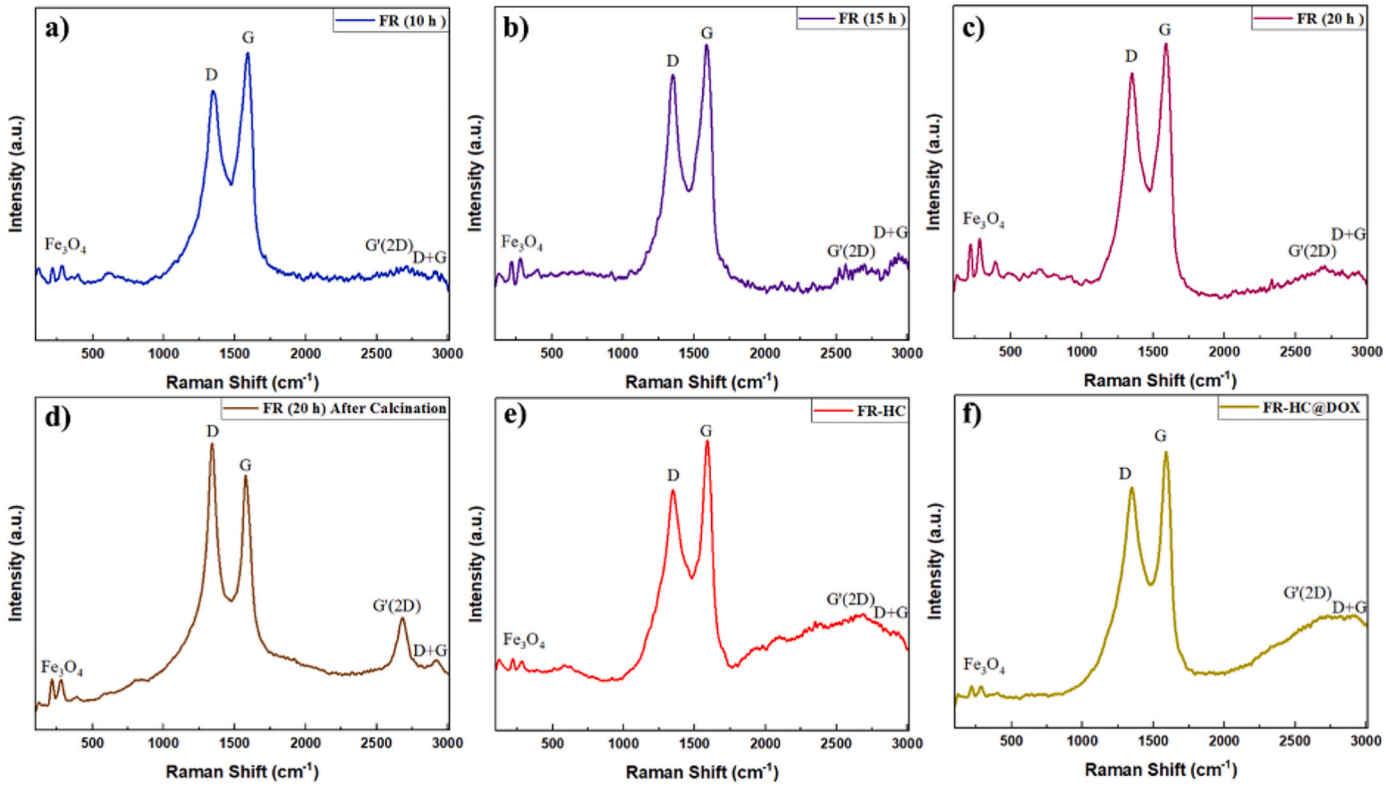


Fig. 3. Raman Spectra of the (a–c) FR for 10, 15, and 20 h, (d) FR for 20 h after calcination, (e) FR-HC, and (f) FR-HC@DOX.

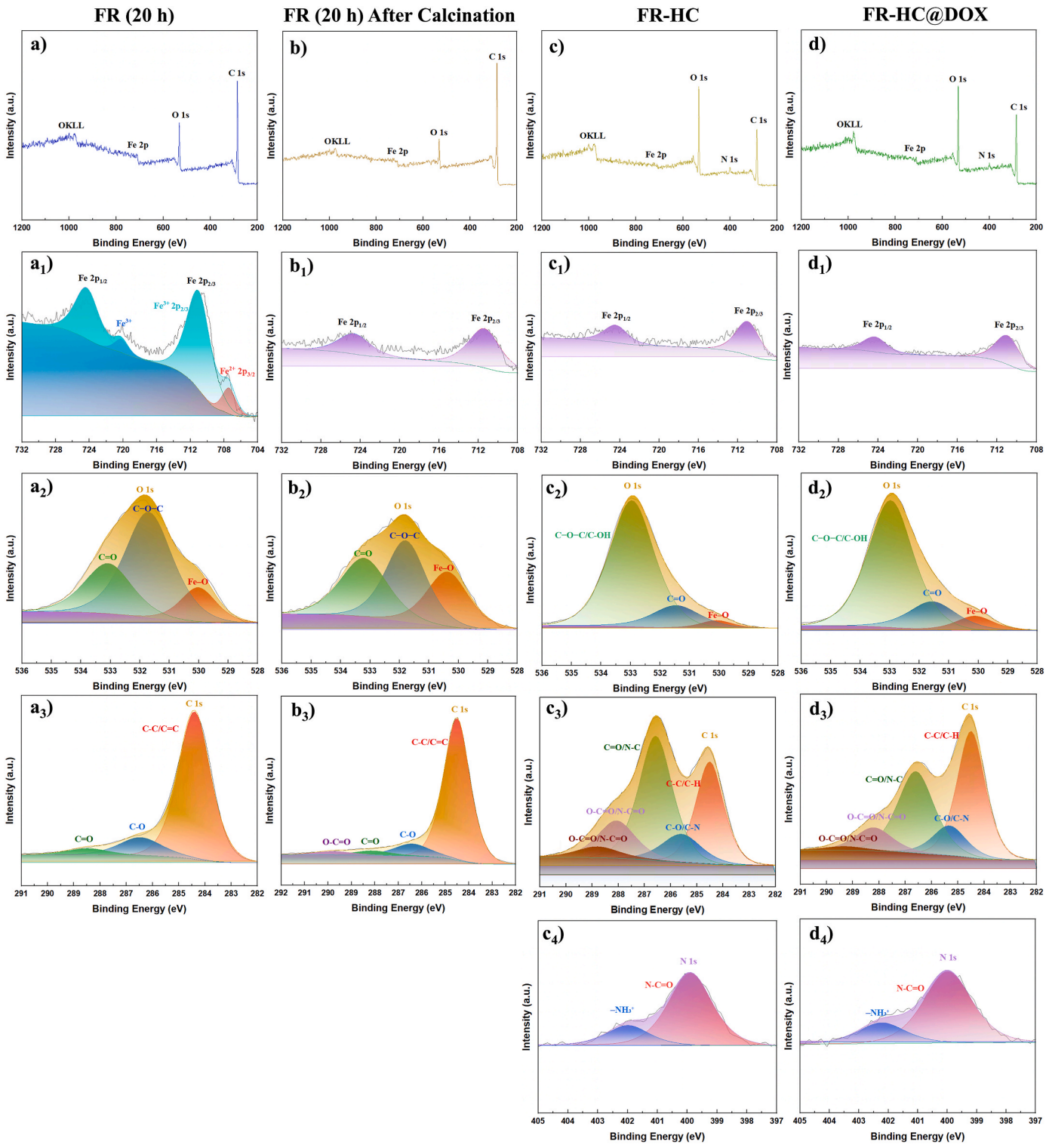


Fig. 4. XPS survey spectra of (a) FR (20 h), (b) FR (20 h) after calcination, (c) FR-HC, and (d) FR-HC@DOX MNPs; and their corresponding high-resolution spectra of (a_1–d_1) Fe 2p, (a_2–d_2) O 1s, (a_3–d_3) C 1s, and (c_4–d_4) N 1s regions.

iron. In Fig. 4a_1, Fe $2p_3/_2$ and Fe $2p_1/_2$ peaks are observed at approximately 710.5 eV and 724.0 eV, these values are characteristic of the mixed oxidation states Fe^{2+} and Fe^{3+} present in magnetite Fe_3O_4. After calcination which is shown in Fig. 4b_1, these peaks become sharper and more defined, while in the polymer-functionalized samples Fig. 4c_1, d_1, the Fe 2p signal becomes slightly broader and less intense, likely due to encapsulation and surface modification which reduces direct Fe detection [51], in FR-HC and FR-HC@DOX (Fig. 4c_1 and 4d_1), Fe peaks broadened and decreased in intensity, a typical effect of polymer encapsulation reducing direct Fe surface exposure, A similar effect has been reported for Fe_3O_4–rGO by Scaria et al. [52] and Fe_3O_4/chitosan–polypyrrole composites by Yin et al. [53], but in this case the attenuation is more pronounced, reflecting thicker multilayer coverage. The O 1s spectra given in Fig. 4a_2–d_2 provide insights into oxygen environment. As illustrated in Fig. 4a_2, three peaks are detected which is lattice oxygen Fe–O, C=O, and C–O–C, at (530.1, 531.5, and 532.8 eV).

As seen in Fig. 4b$_2$, the C–O–C contribution decreases after calcination, while in Fig. 4c$_2$ and Fig. 4d$_2$, the Fe–O signal weakens, and polymer-associated peaks become more prominent. This indicates effective surface modification with oxygen-rich groups from HA, CHI, and DOX, further supported by peak shifts and area changes [50,53,54]. C 1s spectra in Fig. 4a$_3$–d$_3$ reveal the carbon bonding states. The initial sample in Fig. 4a$_3$ shows peaks for sp^2-hybridized C=C/C–C, C–O, and O–C=O at (284.6, 285.5, and 288.6 eV). After calcination, Fig. 4b$_3$, slight shifts suggest thermal reduction of surface oxygen groups. In contrast, the polymer-coated samples in Fig. 4c$_3$ and 4d$_3$ exhibit multiple new components, including C–N, C=N, and C–O–C [50,54], consistent with the presence of chitosan and DOX, both rich in amine and glycosidic linkages. The growing intensity of oxygen and nitrogen bonded carbon peaks confirms dense organic layer deposition. The N 1s spectra in Fig. 4c$_4$ and 4d$_4$ offer direct evidence of nitrogen incorporation. The observed peaks around 400–402 eV are attributed to amine groups (–NH_2 or –NH_3^+) and N–C=O bonds, associated with CHI and DOX [53,54]. The more pronounced signal in Fig. 4d$_4$ reflects additional nitrogen from DOX, suggesting successful loading and stable integration into the multilayer structure.

Compared to bare FR, the coated systems show a clear decrease in Fe signal intensity, reflecting effective surface shielding by HA, CHI, and DOX layers. The increase in C and the emergence of N confirm progressive organic layer deposition and drug incorporation. Oxygen contributions also redistribute from lattice Fe–O toward C–O and C=O bonds, consistent with polysaccharide and drug functional groups. The extent of Fe attenuation and N enrichment in the system is more pronounced than in previously reported [52,53], underscoring the superior encapsulation density and stability achieved by the LbL multilayer design.

The FT-IR spectra of FR, FR-HC and FR-HC@DOX samples are shown in Fig. 5. When the spectra of FR, FR-HC and FR-HC@DOX are examined, the presence of iron nanoparticles in their structures is shown a peak at 560 cm^{-1}, while the band observed at 1550 cm^{-1} may belong to the skeletal vibration ($\nu_{C=C,\ C\text{-}C}$) of the graphene layers in the spectrum [55]. The characteristic peaks observed at 3300, 2860, and 1040 cm^{-1} in the FTIR spectra of FR-HC and FR-HC@DOX nanoparticles, attributable to HA and CS, correspond to the stretching vibrations of hydroxyl (O–H) groups, C–H bonds, and C–O bonds [28]. The FT-IR analysis confirmed the successful LbL coating of HA, CHI, and DOX on FR nanoparticles. These results are consistent with previous reports on CS/HA/κ-carrageenan MNPs [28] and Fe_3O_4/rGO nanocomposites [55], where similar peaks confirmed polymer coating and nanoparticle stabilization. The spectra verify that the LbL functionalization and DOX loading were successfully achieved.

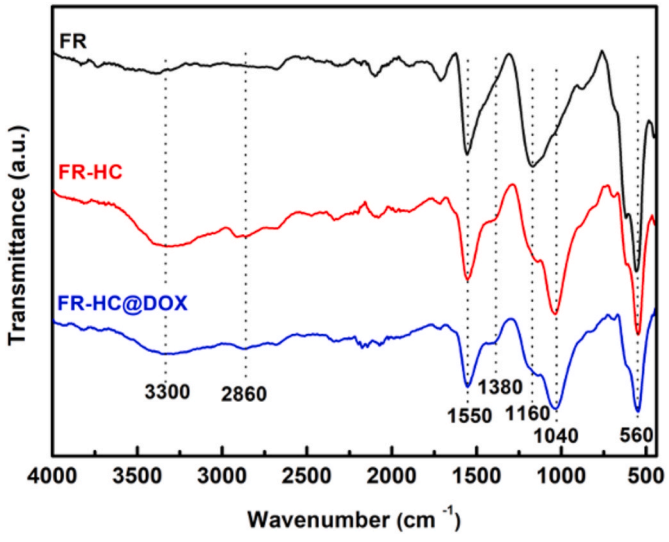


Fig. 5. FTIR spectra of FR (20 h) after calcination, FR-HC, and FR-HC@DOX MNPs.

3.2. VSM measurements and zeta potential of the samples

The magnetic properties of the synthesized FR nanoparticles at various reaction durations were assessed using VSM, and the resulting hysteresis curves are depicted in Fig. 6a–e. The saturation magnetization (M_s) of the calcined FR samples demonstrated a progressive increase with longer synthesis durations, reaching values of 35.08 emu/g for the 10 h, 38.47 emu/g for the 15 h, and 43.87 emu/g for 20 h samples. This enhancement in magnetic performance is attributed to improved crystallinity and the enlargement of magnetic domains facilitated by prolonged thermal and chemical reaction times, which promote more uniform and well-ordered magnetic spin alignment within the Fe_3O_4 phase [11,56]. The corresponding remanent magnetization (M_r) values were measured as 8.35 emu/g for the 10 h, 9.39 emu/g for the 15 h, and 11.15 emu/g for the 20 h. Although M_r also increased with synthesis time, the relative increment is less pronounced compared to M_s. This may be due to a partial reduction in magnetic anisotropy caused by particle size growth and interparticle interactions, which can suppress magnetic once the external magnetic field is removed [55,57]. The coercivity (H_c) also followed an increasing trend with synthesis time, measured as 79.74 Oe, 89.82 Oe, and 104.87 Oe for the 10 h, 15 h, and 20 h samples, indicating enhanced resistance to demagnetization due to improved structural rigidity and particle integrity [38,50]. After coating FR-HC sample the M_s and M_r values decreased to 41.90 emu/g and 10.32 emu/g, as shown in Fig. 6d, and by loading with DOX, the resulting FR-HC@DOX nanocarriers exhibited a notable reduction in magnetic response, with M_s and M_r dropping to 26.04 emu/g and 6.63 emu/g as shown in Fig. 6e. This decline is expected and primarily attributed to the diamagnetic nature of the drug molecules, which form a surface coating around the magnetic cores. This coating introduces a non-magnetic barrier that disrupts spin exchange interactions at the surface and reduces the overall magnetic moment of the composite [58]. As reported by Jiang et al. [59], Fe_3O_4/chitosan–polyacrylamide composites exhibited a pronounced suppression in M_s, decreasing from ~66.5 emu/g for bare Fe_3O_4 to 8.85–5.74 emu/g after polymer encapsulation, while maintaining superparamagnetic-like coercivity. Similarly, Le et al. [60] demonstrated that Fe_3O_4–DOX conjugates showed a reduction of M_s from ~60 emu/g to ~46 emu/g in one layer deposition due to the diamagnetic nature of DOX yet preserved stable hysteresis behavior suitable for biomedical applications. Compared to these systems, The FR-HC@DOX nanocarriers retained a higher M_s (26.04 emu/g), indicating that the LbL HA/CHI architecture provides a more favorable balance between magnetic responsiveness and drug encapsulation. The coercivity values for FR-HC and FR-HC@DOX were recorded as 94.15 Oe and 93.40 Oe, indicating that the drug loading process slightly softens the magnetic response, but the core structural stability remains largely unaffected. These FR-HC@DOX MNPs can be referred in soft ferromagnetic character [11]. The zoomed-in views in Fig. 6a$_1$–e$_1$ highlight the nuanced variations in coercivity and remanence, further supporting the influence of synthesis duration, calcination, and surface functionalization on the magnetic behavior of the FR nanoparticles. Based on the reported studies, the preferred M_s range for slightly coated MNPs is between 20 and 70 emu/g for magnetic drug delivery, hyperthermia, and resonance imaging applications [8,11,56,61] which means that FR-HC@DOX MNPs synthesized in this study with multilayered coatings are obtained in the ideal magnetic saturation value.

Zeta potential measurements were used to understand how the surface charge of FR nanoparticles changes during different stages of synthesis and surface coating (Fig. 7). The nanoparticles for 10 h synthesis had a strong negative charge of −30.3 mV, which means they were very stable in liquid and had many oxygen-containing groups on their surface. When the reaction time was increased to 15 h and 20 h (−22.8 mV, −21.5 mV), the negative charge became a bit weaker. This shows that

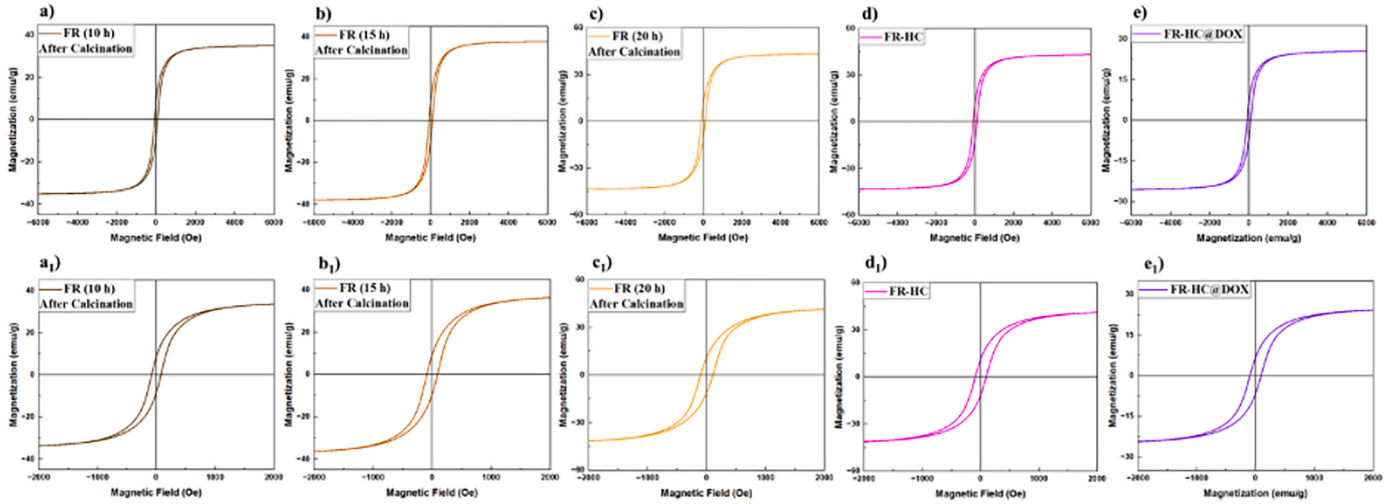


Fig. 6. VSM hysteresis curves of the (a–c) FR samples synthesized at 10 h, 15 h, and 20 h for after calcination; (d) FR-HC and (e) FR-HC@DOX samples. (a_1–e_1) Corresponding zoomed-in views of the low-field region.

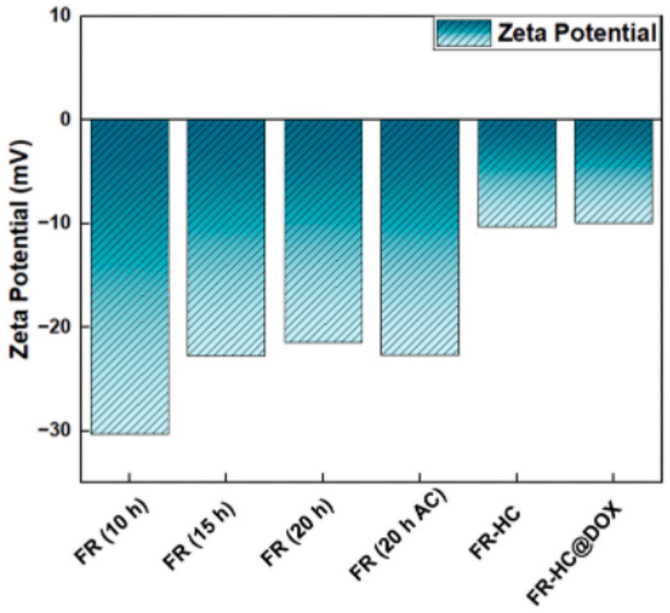


Fig. 7. Zeta potential measurements of the FR samples synthesized at 10 h, 15 h, and 20 h. FR (20 h) after calcination, FR-HC and FR-HC@DOX MNPs.

longer synthesis reduced the oxygen groups, making the surface less negative After 20 h calcination (AC) of the FR nanoparticles (FR (20 h)), the zeta potential remained almost the same at −22.7 mV, showing that the structure changed but the surface charge stayed similar [11,62]. When the nanoparticles were coated with hyaluronic acid and chitosan (FR-HC), the charge changed a lot, reaching −10.3 mV. This is due to chitosan has positively charged amine groups, and HA is negatively charged. Together, they balance out the surface charge and make it less negative [63]. When DOX was added in the last HA layer (FR-HC@DOX), the surface charge became −9.9 mV, which is very close to the previous step [64]. This means that the DOX did not strongly change the surface charge, probably because it was covered by the HA layer. The coating process made the surface less negative which is more biocompatible, less toxic, stable in circulation due to repulsion between particles, preventing aggregation, longer circulation time in the bloodstream, and good for passive targeting via the enhanced permeability and retention (EPR) effect in tumors.

3.3. TEM analyses of the samples

To investigate the morphological features and elemental distribution of the FR (20 h) after calcination and after coating FR-HC@DOX, TEM/STEM coupled with EDX) was performed (Fig. 8). In the FR sample, the TEM/STEM images at various magnifications (Fig. 8a–e) reveal a loosely agglomerated nanostructure composed of uniformly dispersed Fe_3O_4 nanoparticles anchored onto rGO sheets. The Fe_3O_4 nanoparticles are relatively spherical, and their distribution suggests good nucleation across the graphene substrate without significant aggregation into large clusters. Elemental mapping (Fig. 8f–j) confirms the presence and uniform distribution of iron (Fe), oxygen (O), and carbon (C), which correspond to the expected constituents of Fe_3O_4 and the rGO support. The merged EDX maps indicate strong elemental overlap, signifying good compositional homogeneity within the composite matrix [50]. Upon functionalization with a LbL coating of HA, CHI, and DOX, distinct morphological changes were observed in the FR-HC@DOX MNPs (Fig. 8k–p). The TEM images show a clear core shell structure, in which Fe_3O_4 cores are encapsulated by a polymeric shell, confirming the successful surface modification. This coating process appears to suppress agglomeration. The successful formation of the nanocarrier structure is especially evident in Fig. 8m–p, where the shell layers are visibly surrounding the magnetic cores. As shown in Fig. 8w–y, the coating thickness increased progressively, measuring ~1.5 nm after the first coating cycle, ~2.5 nm after the second coating cycle, and ~4 nm after the third coating LbL cycle, indicating that each additional layer contributes an average thickness of about 1.5 nm. Wenfa Yu et al. [65] reported that HA/CHI multilayers exhibited a thickness increment of ~12 nm per bilayer (~6 nm per individual layer). The elemental mapping of FR-HC@DOX as demonstrated in Fig. 8q–v confirms the spatial distribution of Fe, O, C, and N. The strong nitrogen signal provides direct evidence for the incorporation of CHI and DOX, both of which contain nitrogenous amine functional groups. The uniform spatial overlap of these elements suggests a well-dispersed and stable coating over the Fe_3O_4 core, with no observable phase separation or irregular aggregation [43]. The histogram presented in Fig. 8w, derived from particle size analysis of Fig. 8m, indicates an average particle diameter of approximately 25 nm. This relatively small and uniform size distribution is advantageous for biomedical applications, particularly in targeted drug delivery where size influences biodistribution and cellular uptake. These results confirm that the LbL assembly not only alters the surface chemistry, but also improves the overall morphology, producing a more compact, stabilized, and uniformly coated nanocarrier system.

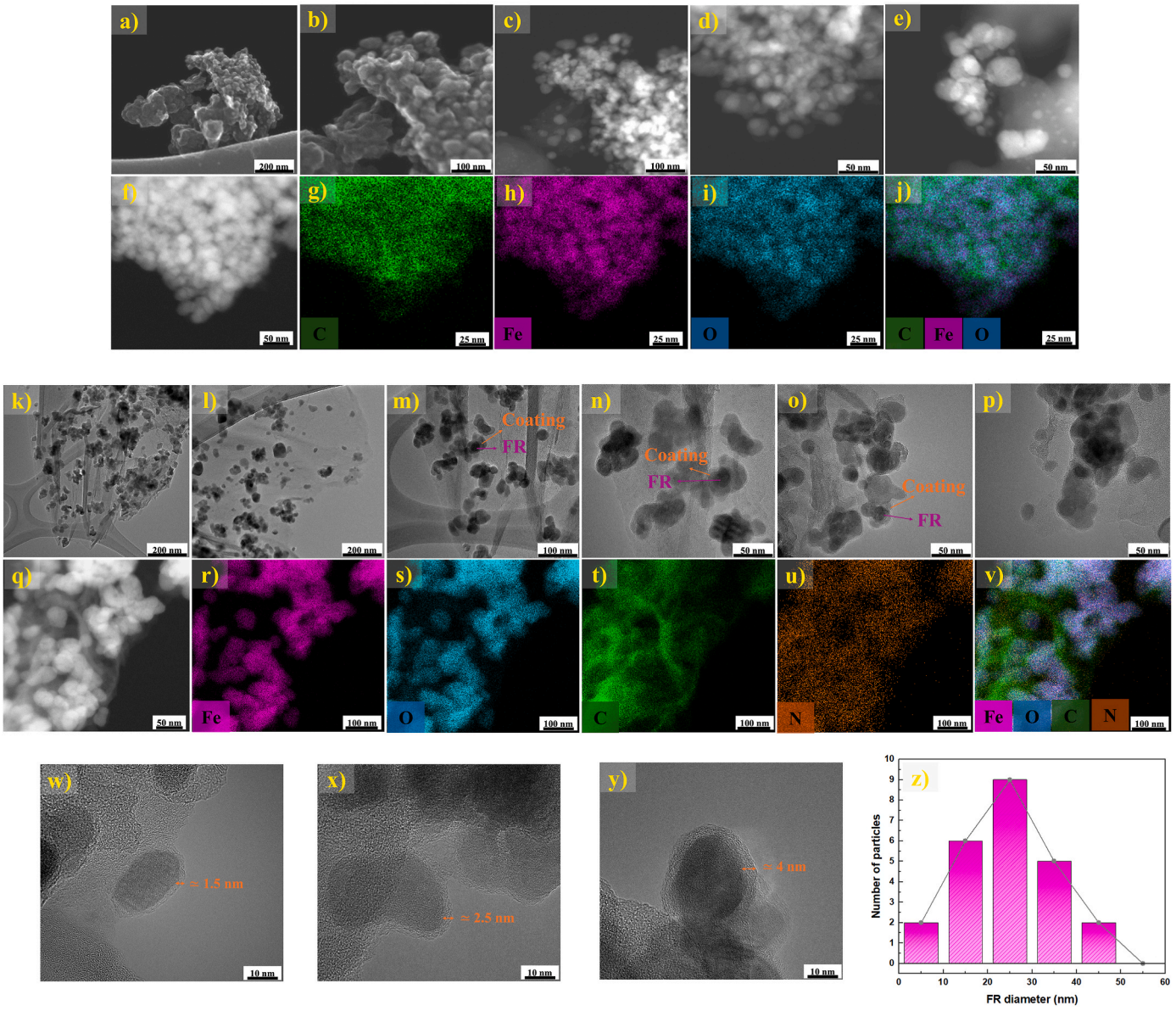


Fig. 8. (a–e) STEM/TEM images of FR samples at various magnifications, (f–j) corresponding EDX elemental maps, (k–p) STEM/TEM images of FR-HC@DOX sample, (q–v) elemental mapping of FR-HC@DOX samples, (w–y) thickness of coating for (first, second, and third deposition), and (z) Particle size distribution of FR (20 h) calculated from TEM images (m).

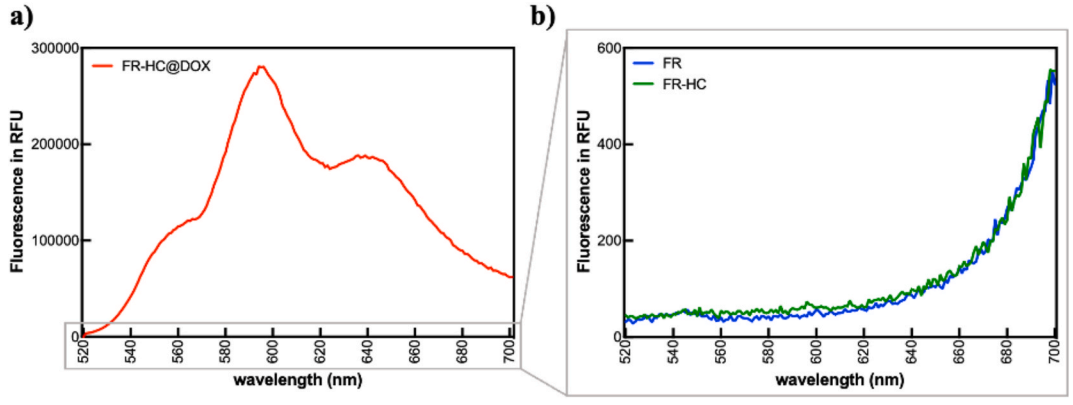


Fig. 9. Drug loading analysis of the FR, FR-HC, and FR-HC@DOX MNPs using fluorescence spectroscopy. Nanoparticles were excited at 470 nm and emission spectra were collected in the 520–700 nm range. Fluorescence spectra of all nanoparticles (a) and close-up view of FR and FR-HC nanoparticles (b).

3.4. Fluorometric analysis of samples

Fluorescence spectroscopy was employed as a rapid and straightforward method to evaluate DOX loading to the nanoparticles. Fluorescence measurement was designed according to the fluorometric properties of DOX. Based on the obtained spectra, neither FR nor FR-HC nanoparticles exhibited detectable fluorescence emission within the 520–700 nm range when excited at 470 nm, indicating the absence of fluorescence signal in this interval (Fig. 9a-b). On the other hand, the DOX-loaded FR-HC@DOX MNPs exhibited a strong fluorescence emission centered around 600 nm, as expected for DOX (Fig. 9a) [66]. The pronounced fluorescence signal at 600 nm confirms the successful loading of DOX onto the nanoparticle structure [67]. A secondary emission peak was detected near 640 nm, which is consistent with previously reported spectral shifts observed under specific conditions such as changes in solvent polarity, pH, or molecular aggregation [32, 68].

3.5. Evaluation of drug content and in vitro release kinetics of FR-HC@DOX samples

DOX was chosen as the model drug for the *in vitro* release study owing to its broad-spectrum anticancer activity. The amount of drug incorporated per layer was quantified by synthesizing the nanoparticles as described in Section 2.2, considering the respective number of coatings, and subsequently determining both the DLC and DLC (%). The DLC and DLC (%) of FR-HC@DOX at each coating layer were quantified at 484 nm using a UV–Vis spectrophotometer, based on a calibration curve prepared in DMSO, a solvent known to enhance DOX release. Both DLC and DLC (%) increased progressively with the number of coating layers, reflecting higher absolute DOX content and improved loading efficiency (Fig. 10). Single-layer nanoparticles contained approximately 31 μg of DOX, whereas two- and three-layer nanoparticles exhibited increased loading of 40 μg and 46 μg, indicating that each additional layer contributes to the overall drug retention capacity. Similarly, the DLC (%) increased with the number of layers, rising from 3.1 % for single-layer particles to 4.0 % for particles with two layers and 4.6 % for those with three layers. These findings suggest that multilayer coatings not only enhance the absolute drug load but also optimize nanoparticle loading efficiency and supporting controlled and highly efficient drug delivery.

The release profiles of DOX at different time intervals and under two different pH conditions (pH 7.4 and pH 5.5) are presented in Fig. 11. As observed, DOX release is influenced by the pH of the medium, which has a significant impact on the cumulative release of the drug. The release of DOX from FR-HC@DOX occurs much more rapidly at pH 5.5 compared to pH 7.4. After 56 h, the cumulative release of DOX reached almost 100

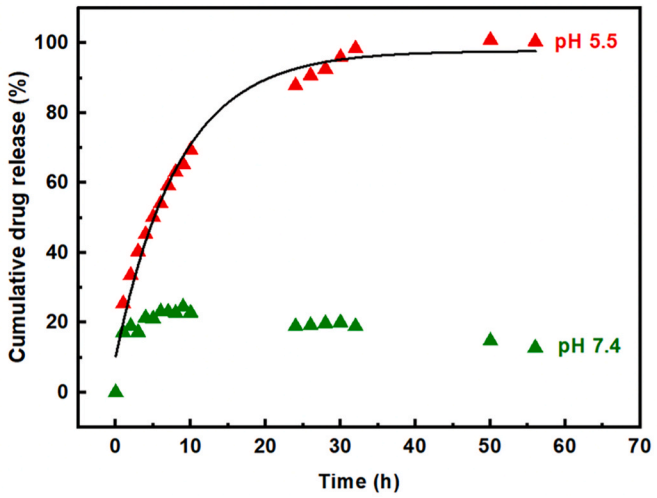


Fig. 11. Cumulative release profile of DOX from FR-HC@DOX MNPs at pH 7.4 and pH 5.5.

% at pH 5.5, whereas only 13 % was released at pH 7.4. This can be attributed to the pH-sensitive nature of HA and CHI [69]. These results are consistent with previous reports [70], confirming that the pH-responsive release behavior of FR-HC@DOX allows for accelerated drug release under acidic conditions, which is advantageous for targeted delivery in tumor-like microenvironments.

The release kinetics of DOX from the FR-HC@DOX MNPs under acidic (pH 5.5) and physiological (pH 7.4) conditions were evaluated using the zero-order (Figs. 12a and 13a), first-order (Figs. 12b and 13b), Higuchi (Figs. 12c and 13c), and Korsmeyer–Peppas (Figs. 12d and 13d) models. The data showed stronger correlation with the Higuchi and Korsmeyer–Peppas models, indicating that diffusion is the dominant release mechanism under both acidic and physiological conditions. This finding is consistent with Kahraman and Nasun-Saygili's report on 5-FU-loaded GO/HAp composites, where drug release also followed Higuchi and Korsmeyer–Peppas kinetics at acidic pH, while zero-order behavior was more evident at physiological pH [71]. The kinetic evaluation of DOX release from the FR-HC@DOX MNPs under different pH conditions revealed distinct behaviors, highlighting the system's pH-responsiveness (Table 1).

Under acidic conditions (pH 5.5), the Korsmeyer–Peppas model showed the highest correlation with the release data (R^2 = 0.9743; Fig. 12d), with a release exponent of n = 0.3537, indicative of Fickian diffusion. The observed Fickian diffusion-controlled release of DOX from the FR-HC@DOX MNPs under acidic conditions indicates a predictable

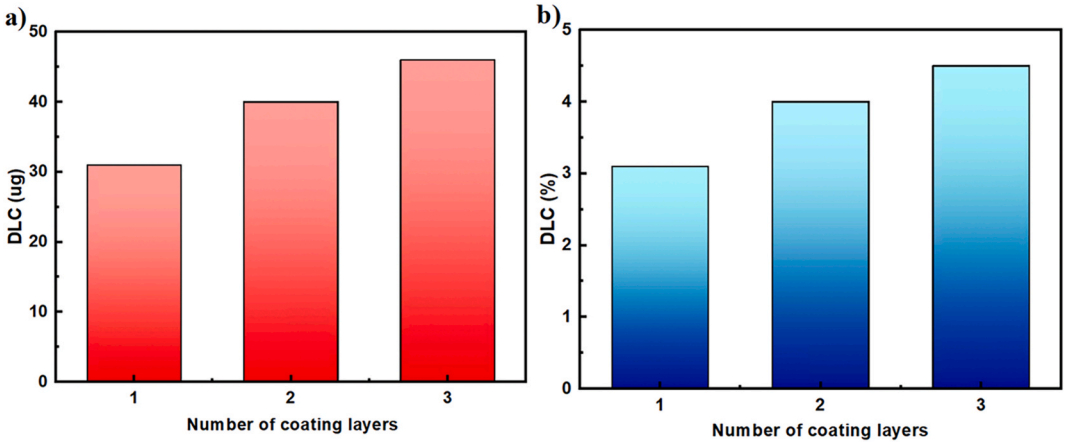


Fig. 10. DLC (a) and DLC (%) (b) of FR-HC@DOX MNPs as a function of coating layer number.

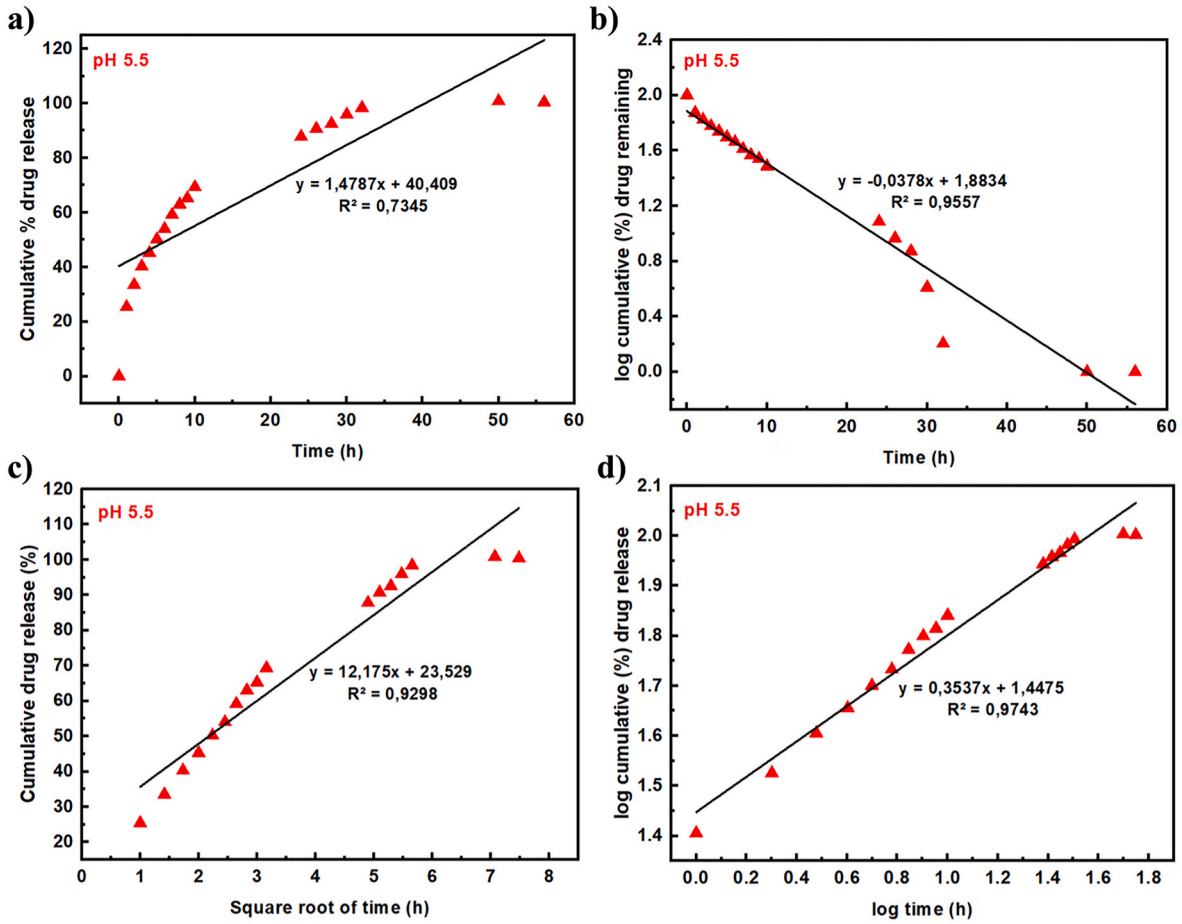


Fig. 12. Linear fitting of DOX release profiles from FR-HC@DOX MNPs in pH 5.5 PBS at room temperature. (a) Zero-order kinetic model, (b) First-order kinetic model, (c) Higuchi kinetic model, and (d) Korsmeyer–Peppas kinetic model.

Table 1
Mathematical models and parameters of drug release from FR-HC@DOX MNPs at room temperature under different pH conditions.

Kinetic Model	Mathematical Equation[a]		pH	
			5.5	7.4
Zero-order	$M_t = M_0 + k_0 t$	k_0 (h^{-1})	1.4787	−0.0471
		R^2	0.7345	0.0209
First-order	$M_t = M_0 e^{-kt}$	k (h^{-1})	−0.0378	3.0×10^{-5}
		R^2	0.9557	0.0002
Higuchi	$M_t = k_H \sqrt{t}$	k_H ($h^{-1/2}$)	12.175	−0.8206
		R^2	0.9298	0.2767
Korsmeyer-Peppas	$\frac{M_t}{M_\infty} = kt^n$	n (h^{-1})	0.3537	−0.0492
		R^2	0.9743	0.1147

[a] M_t: Amount of drug released at time t, M_0: Initial amount of drug, M_∞: Total amount of drug released at infinite time, k_0, k_H, k: Release rate constants for each model, n: Release exponent indicating mechanism in the Korsmeyer-Peppas model.

and controlled drug liberation, which is advantageous for targeted delivery to tumor tissues while minimizing systemic exposure. These results suggest that DOX diffusion through the hydrated polymeric matrix represents the predominant release mechanism in acidic environments. The relatively high correlation with the first-order model ($R^2 = 0.9557$; Fig. 12b) further supports the concentration-dependent nature of the process. Moderate agreement with the Higuchi model ($R^2 = 0.9298$; Fig. 12c) also reinforces the contribution of diffusion, although deviations from linearity imply additional influences such as polymer swelling or structural relaxation. The comparatively lower fit for the zero-order model ($R^2 = 0.7345$; Fig. 12a) indicates that a constant-rate process does not adequately describe the observed profile.

Under physiological conditions (pH 7.4), the correlation coefficients for all kinetic models remained markedly low ($R^2 < 0.3$), reflecting negligible DOX release. The poor agreement of both diffusion-based models (Higuchi, Korsmeyer–Peppas; Fig. 13c, 13d) and concentration-dependent models (first-order; Fig. 13b) suggests that the drug largely remained entrapped within the composite matrix in neutral environments. This behavior can be attributed to reduced solubility and weaker protonation of DOX in neutral media, combined with the structural stability of the FR-HC carrier. The FR-HC@DOX MNPs displayed a strongly pH-dependent release profile, characterized by efficient DOX liberation in acidic environments resembling the tumor microenvironment, while minimizing premature leakage under physiological conditions. Such selective release behavior offers significant therapeutic advantages by promoting drug accumulation at tumor sites and reducing systemic toxicity.

The FR-HC@DOX MNPs exhibit strongly pH-dependent release, with efficient Fickian diffusion-controlled DOX release under acidic conditions resembling the tumor microenvironment, while showing minimal release at physiological pH, thereby enabling targeted delivery and reducing systemic exposure. Based on reported studies, chitosan-coated ZnO nanocarriers enhanced the antibacterial performance of gentamicin by leveraging chitosan's biocompatibility and charge-mediated interactions [72], and these findings highlight improvement of pH-responsive release behavior, supporting the potential of this system for selective drug delivery.

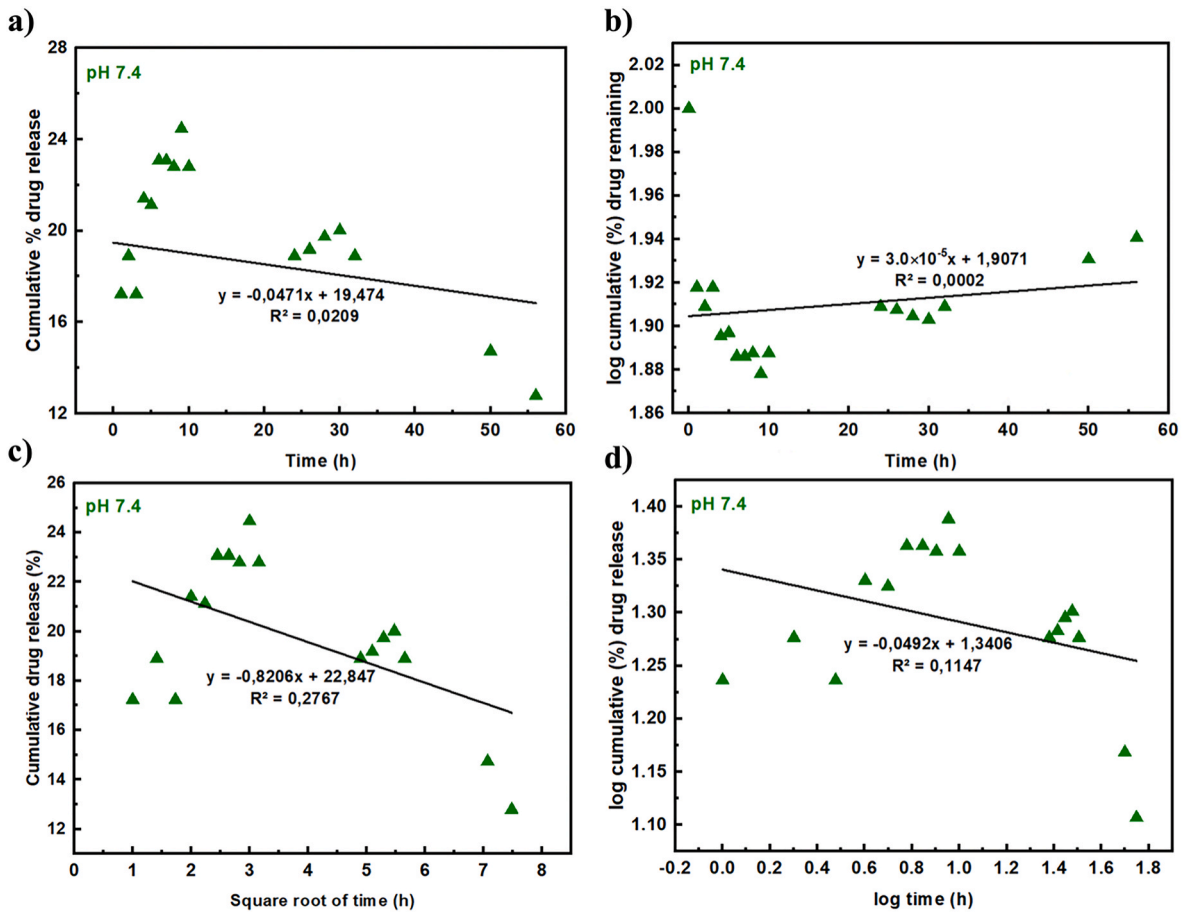


Fig. 13. Linear fitting of DOX release profiles from FR-HC@DOX MNPs in pH 7.4 PBS at room temperature. (a) Zero-order kinetic model, (b) First-order kinetic model, (c) Higuchi kinetic model, and (d) Korsmeyer–Peppas kinetic model.

3.6. Assessment of nanoparticle-induced cytotoxicity and cellular internalization

Biocompatibility of the nanoparticles was assessed by MTT cell viability assay in the 0.02–80 μg/ml dosage interval for up to 48 h. Because MCF-7 cell line is widely accepted as a model system for pre-clinical testing [73], it was selected as the model system for evaluation. In parallel, the effect of nanoparticle treatment was also studied in MCF-12A healthy control breast epithelial cells to compare any difference between cancer and healthy conditions. Application dosages were determined according to similar study [74]. The experiments revealed MNP precipitation at the bottom of the assay plate, which forms an optical barrier and leads to measurement errors. For this reason, a no-cell condition was also used, which was then subtracted from the assay conditions. Cytotoxicity assay revealed that the FR nanoparticles exhibited no cytotoxic effect on either MCF-7 or MCF-12A cells in the dose interval tested (Fig. 14). The relatively low solubility of the FR nanoparticles led to high variability among replicates, resulting in large error bars in the MTT assay. While FR-HC nanoparticles resulted in mild cytotoxicity upon treatment for more than 6 h in MCF-7 cells (Fig. 14a), MCF-12A cells recovered from FR-HC toxicity in the long-term exposure (Fig. 14b). On the other hand, DOX-loaded nanoparticles exhibited higher toxicity in both cancer and healthy cells at higher doses upon prolonged treatment, compared to both FR and FR-HC treated cells (Fig. 14). Although the no-cell control data was subtracted from the actual data to eliminate the effect of nanoparticles forming a physical barrier to light passage, it appears that the nanoparticles, especially FR, bind more strongly to cells than to the surface of the cell culture plates, which results in increased absorbance signal. The increased absorbance signal, which correlates with increasing nanoparticle dosage, appears to reflect a false-positive increase in cell survival.

To evaluate the cell death mechanism upon nanoparticle treatment, MCF-12A healthy control breast epithelial cells were treated with FR-HC or FR-HC@DOX MNPs for 24 h and analyzed by Annexin V staining using flow cytometry to be able to observe apoptosis induction (Fig. 15). Untreated control cells displayed minimal Annexin V positivity, indicating negligible baseline apoptosis. In contrast, treatment with both nanoparticle formulations resulted in a marked increase in apoptotic populations. Specifically, cells treated with FR-HC exhibited ~32 % early and ~10 % late apoptosis, whereas FR-HC@DOX induced ~37 % early and ~39 % late apoptosis, suggesting a more pronounced pro-apoptotic effect (Fig. 15a). Quantitative analysis of Annexin V–positive cells demonstrated a significant increase in apoptosis following nanoparticle treatment under both FR-HC and FR-HC@DOX conditions (Fig. 15b). FR-HC@DOX exhibited a more pronounced pro-apoptotic effect compared to FR-HC, as expected. These results align with Liang et al.'s study [75] in which HA-coated DOX-Fe_3O_4 nanoparticles enhanced cellular uptake and induced stronger apoptosis in drug-resistant MCF-7/ADR cells compared with free DOX or DOX-Fe_3O_4. These results demonstrate that both nanoparticle formulations trigger apoptosis in cancer cells, although to different extents. The stronger effect observed in FR-HC@DOX condition stems from the presence of DOX.

To evaluate the cellular internalization of the nanoparticles as well as the loaded DOX, immunofluorescence analysis was performed utilizing the intrinsic fluorescence property of DOX, as shown in Fig. 16. Bright field visualization was also performed to observe the cytoplasm of the cells. The overlay of bright field and fluorescent images revealed that the

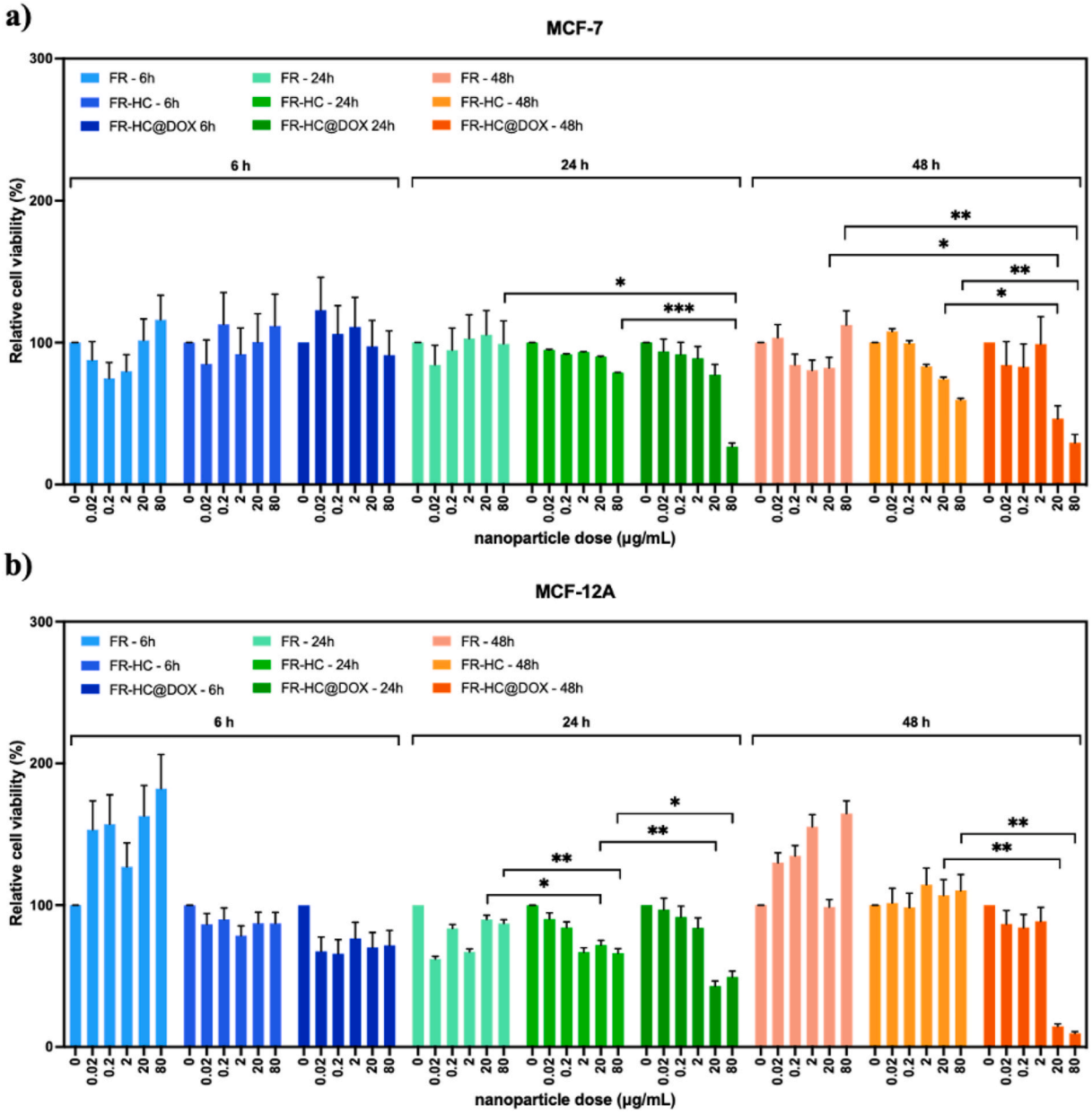


Fig. 14. Cytotoxicity analysis of FR, FR-HC and FR-HC@DOX MNPs in (a) MCF-7 breast cancer, and (b) MCF-12A healthy control breast epithelial cells.

fluorescent signal originates from the intracellular region and DOX was internalized by the cells. DOX was observed in both cytoplasm and nucleus, as it was also observed by other research (Fig. 16c) [76,77]. In addition, DOX was distributed throughout the cytoplasm rather than being restricted to punctate structures. No DOX signal was observed in FR or FR-HC nanoparticles, as expected. Although long-term biocompatibility and *in vivo* studies were not included in the current work, they are crucial for clinical translation and will be the focus of future studies.

4. Conclusion

In this work, Fe_3O_4@rGO (FR) nanoparticles were synthesized with an average particle size of ~25 nm via a solvothermal process, calcined, and subsequently functionalized with alternating HA and CHI layers using an LbL coating strategy. The resulting FR-HC@DOX MNPs had a coating thickness of around 1.5 nm after the first coating cycle, ~2.5 nm after the second cycle, and ~4 nm after the third cycle. They exhibited favorable soft ferromagnetic properties (M_s = 26.04 emu/g; H_c = 93.40 Oe), which are significantly higher than values typically reported for polymer coated and DOX loaded Fe_3O_4 systems (<20 emu/g), indicating that rGO reinforcement preserved magnetic functionality despite multilayer coating.

The incorporation of DOX into the HA layers introduced a strongly pH-sensitive release profile, with nearly 100 % release at pH 5.5 compared to ~13 % at physiological pH 7.4. This contrast in release kinetics surpasses several reported HA based nanocarriers, where acidic release often remains below 80 %, thereby underscoring the efficiency of the multilayer design. Structural and compositional analyses further confirmed uniform elemental distribution and successful integration of rGO, polymer shells, and drug molecules, validating the reproducibility of the synthesis strategy.

Biological evaluation demonstrated that FR and FR-HC nanoparticles maintained excellent biocompatibility in both MCF-7 and MCF-12A cells up to 80 μg/mL, while FR-HC@DOX induced dose and time dependent

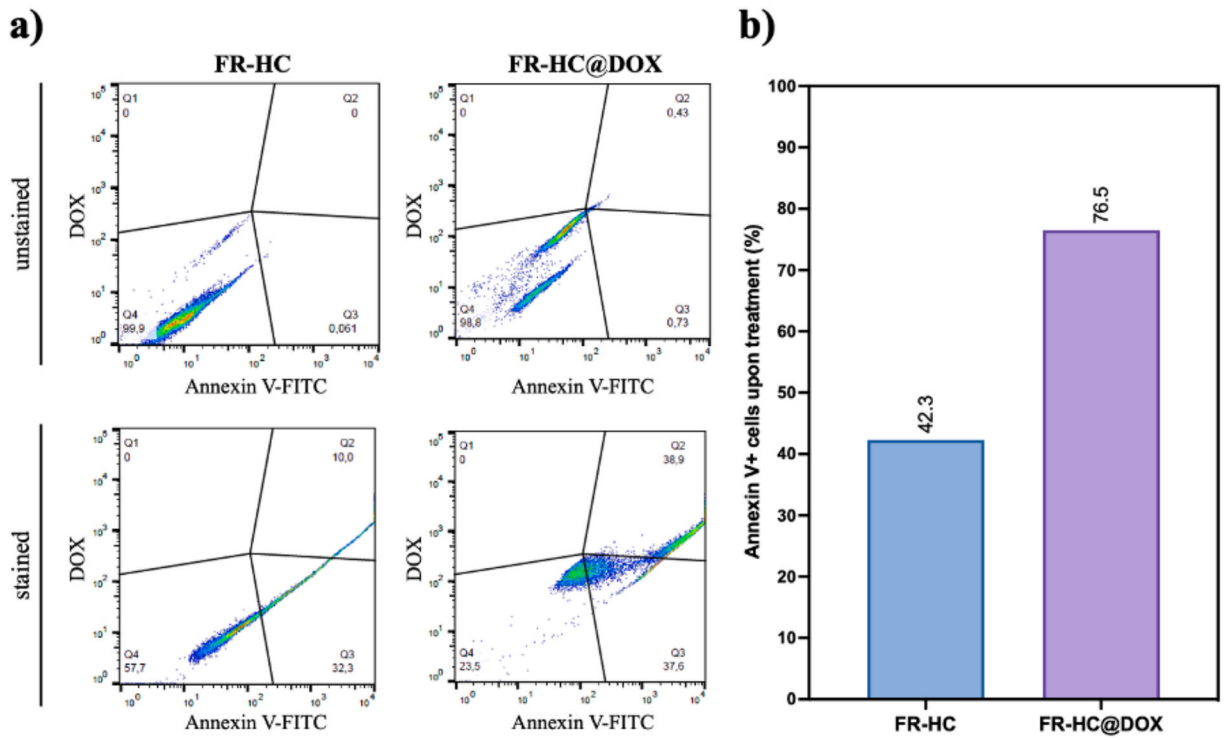


Fig. 15. (a) Representative flow cytometry plots of Annexin V-FITC staining showing apoptosis in MCF-12A cells after treatment with FR-HC or FR-HC@DOX MNPs, and (b) quantitative analysis of Annexin V–positive (Annexin V+) cells demonstrating a significant increase in apoptosis following nanoparticle treatment under both FR-HC (42.3 %) and FR-HC@DOX (76.5 %) conditions compared to control group.

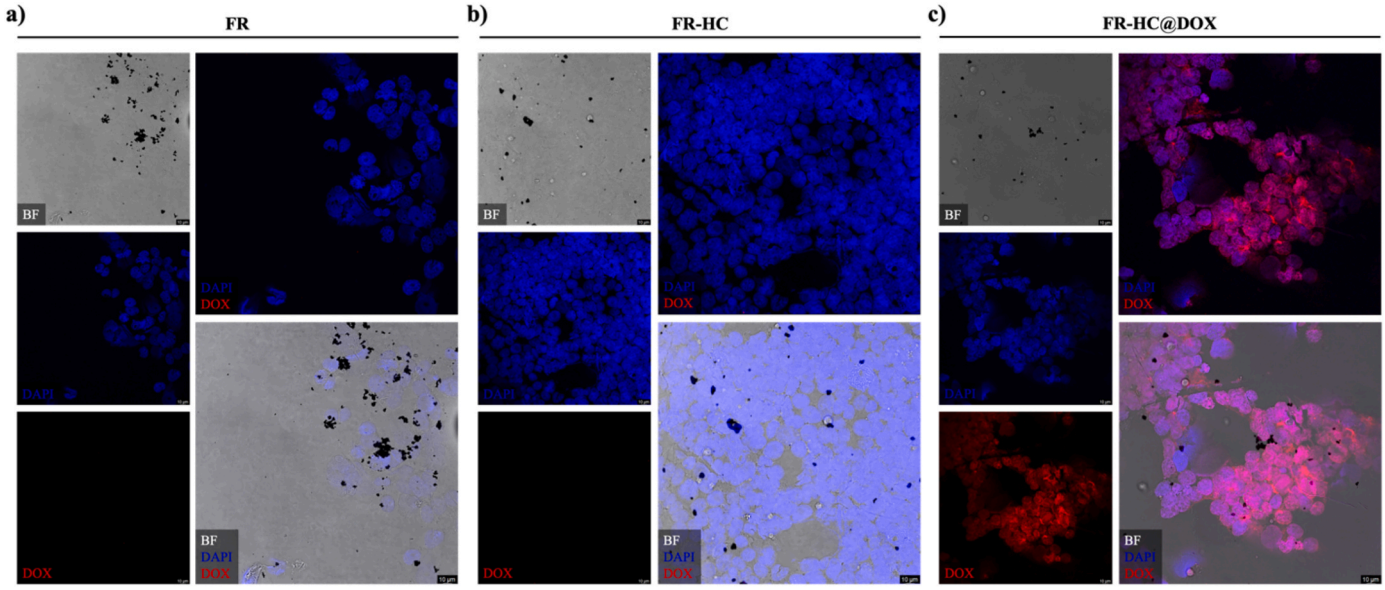


Fig. 16. Cellular uptake analysis of (a) FR, (b) FR-HC, and (c) FR-HC@DOX MNPs using immunofluorescence. DAPI was shown as blue, DOX was used as red and overlapping regions are shown as pink. BF: Bright Field.

cytotoxicity against cancer cells. MCF-7 cell viability decreased by over 60 % within 24 h at 80 μg/mL, highlighting efficient chemotherapeutic delivery. Compared with uncoated Fe_3O_4 systems, which often suffer from aggregation and reduced selectivity, the present platform offers enhanced stability, sufficient magnetic properties, tumor targeting via HA, and controlled therapeutic release, thereby addressing multiple limitations simultaneously. FR-HC@DOX MNPs are synthesized as a multifunctional nanocarrier system that unites structural stability, magnetic guidance, selective targeting, and responsive drug release in a single platform. Future investigations should explore long term stability, *in vivo* biodistribution, and therapeutic efficacy in animal models to accelerate their clinical applicability.

CRediT authorship contribution statement

Aysa Azmoudeh: Writing – original draft, Investigation, Formal analysis. **Seyma Sari:** Writing – original draft, Investigation. **Miray Türk:** Writing – original draft, Investigation. **Sencer Moral:**

Investigation. **Özen Kaya:** Investigation. **Muhammet U. Kahveci:** Writing – original draft, Methodology, Investigation. **Gizem Dinler Doganay:** Writing – original draft, Methodology, Investigation. **Murat Kuşcu:** Writing – review & editing, Investigation. **Nesrin Erkol:** Investigation. **Duygu Ağaoğulları:** Writing – original draft, Supervision, Investigation, Formal analysis, Conceptualization, Project administration.

Declaration of competing interest

The authors declare that they have no known competing financial interests or personal relationships that could have appeared to influence the work reported in this paper.

Acknowledgment

This study was supported by the Scientific Research Projects Department of Istanbul Technical University, with the project number of MYL-2022-44189. This study was also supported by "The Scientific and Technological Research Council of Türkiye (TUBITAK) with project number of 222N330. We express our gratitude to Dr. Sedat Kurnaz from Kastamonu University for conducting the VSM analyses. We also extend our thanks to KUYTAM for their assistance with XPS analyses. Additionally, we appreciate the help from Koç University Nanofabrication and Nanocharacterization Center (n2star) for the TEM analysis. We sincerely thank Deva Holding for kindly providing us with doxorubicin hydrochloride (DOX) for our study.

5 Nomenclature

Abbreviation	Full form/Description
MNPs	Magnetic nanoparticles
Fe_3O_4	Iron oxide (Magnetite)
rGO	Reduced graphene oxide
FR	Fe_3O_4@rGO nanoparticles
HA	Hyaluronic acid
CHI	Chitosan
LbL	Layer-by-Layer assembly
DOX	Doxorubicin
FR-HC	FR coated with HA/CHI multilayers
FR-HC@DOX	FR-HC loaded with doxorubicin
MCF-7	Human breast cancer cell line
MCF-12A	Normal human mammary epithelial cell line
MTT	3-(4,5-dimethylthiazol-2-yl)-2,5-diphenyltetrazolium bromide assay
DLC%	Drug loading capacity percentage
PBS	Phosphate buffered saline solutions

Appendix A. Supplementary data

Supplementary data to this article can be found online at https://doi.org/10.1016/j.jsamd.2025.101012.

References

[1] K.A. Altammar, A review on nanoparticles: characteristics, synthesis, applications, and challenges, Front. Microbiol. 14 (2023) 1155622, https://doi.org/10.3389/fmicb.2023.1155622.
[2] D. Zhang, Q. Tang, J. Chen, Y. Wei, J. Chen, Novel development of Nanoparticles—A promising direction for precise tumor management, Pharmaceutics 15 (2023) 24, https://doi.org/10.3390/pharmaceutics15010024.
[3] K. Chang, C. Podder, H. Pan, Ligand decomposition differences during thermal sintering of oleylamine-capped gold nanoparticles in ambient and inert environments: implications for conductive inks, ACS Appl. Nano Mater. 6 (2023) 23418–23429, https://doi.org/10.1021/acsanm.3c04803.
[4] S. Lin, X. Mi, L. Xi, J. Li, L. Yan, Z. Fu, H. Zheng, Efficient reduction photocatalyst of 4-Nitrophenol based on ag-nanoparticles-doped porous ZnO heterostructure, Nanomaterials 12 (2022) 2863, https://doi.org/10.3390/nano12162863.
[5] S. Căprărescu, G.T. Tihan, R.G. Zgârian, A.M. Grumezescu, C. Lazau, C. Bandas, L. I. Atanase, C.A. Nicolae, Synthesis and characterization of cellulose Acetate/Polyethylene Glycol/Poly(Styrene)-b-Poly(4-Vinylpyridine) membrane embedded with Hydrotermaly activated TiO2 nanoparticles for waste-waters treatment by membrane processes, Polymers 17 (2025) 446, https://doi.org/10.3390/polym17040446.
[6] Y. Ren, Y. Zhang, X. Li, Application of AgNPs in biomedicine: an overview and current trends, Nanotechnol. Rev. 13 (2024) 20240030, https://doi.org/10.1515/ntrev-2024-0030.
[7] H. Ghaznavi, R. Afzalipour, S. Khoei, S. Sargazi, S. Shirvalilou, R. Sheervalilou, New insights into targeted therapy of glioblastoma using smart nanoparticles, Cancer Cell Int. 24 (2024) 160, https://doi.org/10.1186/s12935-024-03331-3.
[8] X. Feng, Y. Xue, S. Gonca, K. Ji, M. Zhang, F.R. García-García, Q. Li, Y. Huang, K. V. Kamenev, X. Chen, Ultrasmall superparamagnetic iron oxide nanoparticles for enhanced tumor penetration, J. Mater. Chem. B 11 (2023) 3422–3433, https://doi.org/10.1039/d2tb02630a.
[9] R.J. Reena, N.A.N. Raj, Multifaceted characterization and therapeutic evaluation of Co-precipitated cobalt ferrite nanoparticles for magnetic hyperthermia cancer therapy, J. Med. Phys. 49 (2024) 510–518, https://doi.org/10.4103/jmp.jmp_57_24.
[10] A.C. Horta, A. Poças, J.S. Amaral, C.O. Amorim, Fine-Tuning of Mn-Ferrite nanoparticle size using a Dual-Base coprecipitation method, Mater. Sci. Eng. B 314 (2025) 118058, https://doi.org/10.1016/j.mseb.2025.118058.
[11] A. Azmoudeh, S. Moral, S. Sari, M. Türk, M.U. Kahveci, G.D. Doganay, D. Ağaoğulları, Magnetic iron-based nanoparticles encapsulated in graphene/reduced graphene oxide: synthesis, functionalization and cytotoxicity tests, J. Sci. Adv. Mater. Devices 9 (2024) 100776, https://doi.org/10.1016/j.jsamd.2024.100776.
[12] E.G. Höfgen, S. Bandyopadhyay, Insights into semi-continuous synthesis of iron oxide nanoparticles (IONPs) via thermal decomposition of iron oleate, Discover. Nano. 20 (1) (2025) 5, https://doi.org/10.1186/s11671-024-04167-6.
[13] F. Dumitrache, A. Criveanu, I. Lungu, C. Fleaca, L. Gavrila-Florescu, I. Morjan, I. Stamatin, A. Balan, V. Socoliuc, B. Vasile, Experimental Study regarding the synthesis of iron oxide nanoparticles by laser pyrolysis using ethanol as sensitizer; morpho-structural alterations using thermal treatments on the synthesized nanoparticles, Coatings 15 (2025) 234, https://doi.org/10.3390/coatings15020234.
[14] O. Aalling-Frederiksen, R.K. Pittkowski, A.S. Anker, J. Quinson, L. Klemeyer, B. A. Frandsen, D. Koziej, K.M.Ø. Jensen, Effect of solvothermal synthesis parameters on the crystallite size and atomic structure of cobalt iron oxide nanoparticles, Nanoscale Adv. 6 (23) (2024) 5939–5948, https://doi.org/10.1039/d4na00590b.
[15] G. Márquez, E. Pérez, V. Sagredo, Structural and magnetic characterization of Ni-Co mixed ferrite nanopowders synthesized via coprecipitation and sol-gel methods, Mater. Res. 27 (2024) e20230347, https://doi.org/10.1590/1980-5373-MR-2023-0347.
[16] E. Akyol, A. Azmoudeh, I.M. Bolhassan, P.K. Isgor, M. Kuscu, Microdroplet-Based communications with frequency shift keying modulation, IEEE Trans Mol Biol Multiscale Commun (2025) 1, https://doi.org/10.1109/TMBMC.2025.3605771, 1.
[17] B. Kichatov, A. Korshunov, V. Sudakov, A. Golubkov, P. Ryapolov, Droplet manipulation in liquid flow using of magnetic micromotors for drug delivery and microfluidic systems, Colloids Surf. A Physicochem. Eng. Asp. 691 (2024) 133891, https://doi.org/10.1016/j.colsurfa.2024.133891.

[18] Y.Z. Pan, W.H. Wang, Y. Huang, C.X. Yi, X. Huang, PEI-coated Fe3O4 magnetic nanoparticles for fast and segregative removal of uric acid from plasma, Dig. J. Nanomater. Biostruct. 17 (2022) 137–143, https://doi.org/10.15251/djnb.2022.171.137.
[19] A. Singh, N. Dowdall, T. Hoare, Poly(Oligo(Ethylene glycol) Methacrylate)-Based polymers in biomedical applications: preparation and applications, Biomacromolecules 26 (7) (2025) 3929–3973, https://doi.org/10.1021/acs.biomac.5c00145.
[20] T. Carvalho, A. da S. Pereira, R.C.F. Bonomo, M. Franco, P.V. Finotelli, P.F. F. Amaral, Simple physical adsorption technique to immobilize Yarrowia lipolytica lipase purified by different methods on magnetic nanoparticles: adsorption isotherms and thermodynamic approach, Int. J. Biol. Macromol. 160 (2020) 889–902, https://doi.org/10.1016/j.ijbiomac.2020.05.174.
[21] A. Pikabea, J. Forcada, Novel approaches for the preparation of magnetic nanogels via covalent bonding, J. Polym. Sci. Polym. Chem. 55 (2017) 3573–3586, https://doi.org/10.1002/pola.28740.
[22] S. Rowland, A. Aghakhani, R.D. Whalley, A.M. Ferreira, N. Kotov, P. Gentile, Layer-by-Layer nanoparticle assembly for biomedicine: mechanisms, technologies, and advancement via acoustofluidics, ACS Appl. Nano Mater. 7 (2024) 15874–15902, https://doi.org/10.1021/acsanm.4c02463.
[23] S. Kumar, P. Kumar, R. Gupta, V. Verma, Electromagnetic interference shielding behaviors of in-situ polymerized ferrite-polyaniline nano-composites and ferrite-polyaniline deposited fabrics in X-band frequency range, J. Alloys Compd. 862 (2021) 158331, https://doi.org/10.1016/j.jallcom.2020.158331.
[24] N. Fukumitsu, Y. Matsumoto, L. Chen, Y. Sugawara, N. Fujisawa, E. Niiyama, S. Ouchi, E. Oe, T. Saito, M. Ebara, Development of layer-by-layer magnetic nanoparticles for application to radiotherapy of pancreatic cancer, Molecules 30 (2025) 1382, https://doi.org/10.3390/molecules30061382.
[25] V.L.S. dos Santos, R.C. Araújo, E.S. Lisboa, A.M. Lopes, R.L. de Albuquerque-Júnior, J.C. Cardoso, C. Blanco-Llamero, T.A. Deshpande, H.O.W. Anderson, R. Priefer, E.B. Souto, P. Severino, Layer-by-layer assembly: a versatile approach for tailored biomedical films and drug delivery, J. Drug Deliv. Sci. Technol. 91 (2024) 105243, https://doi.org/10.1016/j.jddst.2023.105243.
[26] V. Karthika, M.S. AlSalhi, S. Devanesan, K. Gopinath, A. Arumugam, M. Govindarajan, Chitosan overlaid Fe3O4/rGO nanocomposite for targeted drug delivery, imaging, and biomedical applications, Sci. Rep. 10 (2020), https://doi.org/10.1038/s41598-020-76015-3.
[27] B.S. Dash, Y.J. Lu, P. Pejrprim, Y.H. Lan, J.P. Chen, Hyaluronic acid-modified, IR780-conjugated and doxorubicin-loaded reduced graphene oxide for targeted cancer chemo/photothermal/photodynamic therapy, Biomater. Adv. 136 (2022) 212764, https://doi.org/10.1016/j.bioadv.2022.212764.
[28] M.A. Anbardan, S. Alipour, G.R. Mahdavinia, P.F. Rezaei, Synthesis of magnetic chitosan/hyaluronic acid/κ-carrageenan nanocarriers for drug delivery, Int. J. Biol. Macromol. 253 (2023) 126805, https://doi.org/10.1016/j.ijbiomac.2023.126805.
[29] H. Zhao, Y. Wang, J. Qian, M. Yang, C. Liu, W. Xu, X. Li, M. Xiao, W. Luo, A. Suo, Stimulus-responsive doxorubicin-conjugated hyaluronic acid/polypyrrole nanoplatform for targeted photothermal chemotherapy of breast cancer, Int. J. Biol. Macromol. 322 (2025) 146945, https://doi.org/10.1016/j.ijbiomac.2025.146945.
[30] H. Namazi, V. Zeyni, S. Karimi, A L-lysine-coated graphene oxide/magnetic hydroxyapatite/cubic metal-organic frameworks for targeted and pH-controlled release of doxorubicin to cancer cells, Mater. Chem. Phys. 325 (2024) 129781, https://doi.org/10.1016/j.matchemphys.2024.129781.
[31] S. Krishnaveni, K. Parvathi, M.V. Kaveri, Design and characterization of ROS-responsive doxorubicin encapsulated Fe3O4@saponin/polyethyleneimine nanoparticles for targeted drug delivery applications, Inorg. Chem. Commun. 173 (2025) 113858, https://doi.org/10.1016/j.inoche.2024.113858.
[32] T.N. Nguyen, T.T. Nguyen, T.H.L. Nghiem, D.T. Nguyen, T.T.H. Tran, D. Vu, T.B. N. Nguyen, T.M.H. Nguyen, V.T. Nguyen, M.H. Nguyen, Optical properties of doxorubicin hydrochloride load and release on silica nanoparticle platform, Molecules 26 (13) (2021) 3968, https://doi.org/10.3390/molecules26133968.
[33] A. Criveanu, F. Dumitrache, C. Fleaca, L. Gavrila-Florescu, I. Lungu, I.P. Morjan, V. Socoliuc, G. Prodan, Chitosan-coated iron oxide nanoparticles obtained by laser pyrolysis, Appl. Surf. Sci. Adv. 15 (2023) 100405, https://doi.org/10.1016/j.apsadv.2023.100405.
[34] Z. Cai, Y. Wei, M. Wu, Y. Guo, Y. Xie, R. Tao, R. Li, P. Wang, A. Ma, H. Zhang, Lipase immobilized on layer-by-layer polysaccharide-coated Fe3O4 @SiO2 microspheres as a reusable biocatalyst for the production of structured lipids, ACS Sustain. Chem. Eng. 7 (2019) 6685–6695, https://doi.org/10.1021/acssuschemeng.8b05786.
[35] B. Thierry, F.M. Winnik, Y. Merhi, M. Tabrizian, Nanocoatings onto arteries via layer-by-layer deposition: toward the in vivo repair of damaged blood vessels, J. Am. Chem. Soc. 125 (2003) 7494–7495, https://doi.org/10.1021/ja034321x.
[36] Y. Jia, M. Yuan, H. Yuan, X. Huang, X. Sui, X. Cui, F. Tang, J. Peng, J. Chen, S. Lu, W. Xu, L. Zhang, Q. Guo, Co-encapsulation of magnetic Fe3O4 nanoparticles and doxorubicin into biodegradable PLGA nanocarriers for intratumoral drug delivery, Int. J. Nanomed. 7 (2012) 1697–1708, https://doi.org/10.2147/IJN.S28629.
[37] S. Shah, A. Chandra, A. Kaur, N. Sabnis, A. Lacko, Z. Gryczynski, R. Fudala, I. Gryczynski, Fluorescence properties of doxorubicin in PBS buffer and PVA films, J. Photochem. Photobiol., B 170 (2017) 65–69, https://doi.org/10.1016/j.jphotobiol.2017.03.024.
[38] R.F. Abbas, M.J.M. Hassan, A.M. Rheima, Photo-irradiation synthesis of Fe3O4 and GO/Fe3O4 magnetic nanoparticles for tartrazine adsorption: a comparative and reuse studies, Desalination Water Treat. 316 (2023) 168–184, https://doi.org/10.5004/dwt.2023.30184.
[39] I.P.T. Indrayana, L.A. Tjuana, M.T. Tuny, Kurnia, nanostructure and optical properties of Fe3O4: effect of calcination temperature and dwelling time, in: J. Phys. Conf. Ser., vol. 1341, Institute of Physics Publishing, 2019 082044, https://doi.org/10.1088/1742-6596/1341/8/082044.
[40] L. Stobinski, B. Lesiak, A. Malolepszy, M. Mazurkiewicz, B. Mierzwa, J. Zemek, P. Jiricek, I. Bieloshapka, Graphene oxide and reduced graphene oxide studied by the XRD, TEM and electron spectroscopy methods, J. Electron. Spectrosc. Relat. Phenom. 195 (2014) 145–154, https://doi.org/10.1016/j.elspec.2014.07.003.
[41] A.R. Sarikhani, M. Abedi, S.S. Abolmaali, S. Borandeh, A.M. Tamaddon, Magnetic graphene oxide nanosheets with amidoamine dendronized crosslinks for dual pH and redox-sensitive doxorubicin delivery, BMC Chem 18 (1) (2024) 189, https://doi.org/10.1186/s13065-024-01301-4.
[42] M.A.M. Khan, W. Khan, M. Ahamed, A.N. Alhazaa, Investigation on the structure and physical properties of Fe 3 O 4/RGO nanocomposites and their photocatalytic application, Mater. Sci. Semicond. Process. 99 (2019) 44–53, https://doi.org/10.1016/j.mssp.2019.04.005.
[43] Ö. Balcı-Çağıran, S. Mertdinç-Ülküseven, N. Solati, K. Onbasli, H. Yagci-Acar, D. Ağaoğulları, Plasma-enhanced CVD synthesis and cytotoxic evaluation of graphitic carbon embedded - Fe3O4 nanoparticles, Ceram. Int. 51 (2025) 32684–32692, https://doi.org/10.1016/j.ceramint.2025.05.002.
[44] G. Vinodhkumar, J. Wilson, S.S.R. Inbanathan, I.V. Potheher, M. Ashokkumar, A. C. Peter, Solvothermal synthesis of magnetically separable reduced graphene oxide/Fe3O4 hybrid nanocomposites with enhanced photocatalytic properties, Phys. B Condens. Matter 580 (2020) 411752, https://doi.org/10.1016/j.physb.2019.411752.
[45] H.I. Chu, H.Y. Ho, Y.J. Huang, D.S. Tsai, C.P. Lee, Synthesis of non-planar graphene-wrapped copper nanoparticles with iron(III) oxide decoration for high performance supercapacitors, Nanotechnology 34 (2023) 285401, https://doi.org/10.1088/1361-6528/acca8a.
[46] J. Huang, C. Zong, H. Shen, Y. Cao, B. Ren, Z. Zhang, Tracking the intracellular drug release from graphene oxide using surface-enhanced Raman spectroscopy, Nanoscale 5 (2013) 10591–10598, https://doi.org/10.1039/c3nr03264g.
[47] M. Balcioglu, M. Rana, M.V. Yigit, Doxorubicin loading on graphene oxide, iron oxide and gold nanoparticle hybrid, J. Mater. Chem. B 1 (2013) 6187–6193, https://doi.org/10.1039/c3tb20992j.
[48] B. Scheibe, R. Mrówczyński, N. Michalak, K. Załęski, M. Matczak, M. Kempiński, Z. Pietralik, M. Lewandowski, S. Jurga, F. Stobiecki, Anchoring Fe3O4 nanoparticles in a reduced graphene oxide aerogel matrix via polydopamine coating, Beilstein J. Nanotechnol. 9 (2018) 591–601, https://doi.org/10.3762/bjnano.9.55.
[49] J. Scaria, P.V. Nidheesh, The role of non-radical pathway in heterogeneous activation of persulfate and H2O2 by superparamagnetic magnetite-reduced graphene oxide nanocomposite, Sep. Purif. Technol. 299 (2022), https://doi.org/10.1016/j.seppur.2022.121764.
[50] T. Govindasamy, N.K. Mathew, B. Subramanian, Eco-Friendly enrichment of tainted Fe3O4 nanoparticles and Fe3O4-rGO nanocomposites for superior supercapattery performance, Energy Fuels 38 (21) (2024) 21144–21161, https://doi.org/10.1021/acs.energyfuels.4c03698.
[51] P. Han, C. Wu, J. Tai, H. Zhang, G. Zhao, Q. Chen, Y. Liu, Improved microwave absorption properties of ferrite-rGO composites by covalent bond, J. Alloys Compd. 966 (2023) 171581, https://doi.org/10.1016/j.jallcom.2023.171581.
[52] J. Scaria, P.V. Nidheesh, The role of non-radical pathway in heterogeneous activation of persulfate and H2O2 by superparamagnetic magnetite-reduced graphene oxide nanocomposite, Sep. Purif. Technol. 299 (2022) 121764, https://doi.org/10.1016/j.seppur.2022.121764.
[53] L. Yin, K. Wang, L. Jiang, Y. Xi, Z. Xu, Z. Song, H. Zhou, Green synthesis and adsorption performance of Fe3O4/chitosan/polypyrrole composites for efficient removal of chromium ion, RSC Adv. 15 (2025) 16337–16347, https://doi.org/10.1039/d5ra00872g.
[54] J.B.M. Parambath, K. Vijai Anand, I.M. Ahmady, K. Hasan, H. Alawadhi, H. Lee, C. Han, A.A. Mohamed, Surface modification of magnetite with Carboxyl arylated gold nanoparticles for capture and removal of bacteria, Inorg. Chem. 64 (9) (2025) 4555–4570, https://doi.org/10.1021/acs.inorgchem.4c05588.
[55] N.T.A. Thu, H. Van Duc, N. Hai Phong, N.D. Cuong, N.T.V. Hoan, D. Quang Khieu, Electrochemical determination of paracetamol using Fe3O4/Reduced graphene-oxide-based electrode, J. Nanomater. 2018 (1) (2018) 7619419, https://doi.org/10.1155/2018/7619419.
[56] I. Zarandona, D.M. Correia, J. Moreira, C.M. Costa, S. Lanceros-Mendez, P. Guerrero, K. de la Caba, Magnetically responsive chitosan-pectin films incorporating Fe3O4 nanoparticles with enhanced antimicrobial activity, Int. J. Biol. Macromol. 253 (2023) 126805, https://doi.org/10.1016/j.ijbiomac.2022.11.286.
[57] L.Q. Vo, A.T. Vu, T.D. Le, C.D. Huynh, H.V. Tran, Fe3O4/Graphene Oxide/Chitosan nanocomposite: a smart nanosorbent for Lead(II) ion removal from contaminated water, ACS Omega 9 (15) (2024) 17506–17517, https://doi.org/10.1021/acsomega.4c00486.
[58] I. Najafipour, N. Emami, P. Sadeh, A. Amoli, S. Mosleh-Shirazi, A.M. Amani, H. Kamyab, S. Chelliapan, S.R. Kasaee, E. Vafa, Synthesis of Fe3O4@MIL-101-OH/Chitosan for adsorption and release of doxorubicin, Polym. Test. 142 (2025) 108659, https://doi.org/10.1016/j.polymertesting.2024.108659.
[59] R. Jiang, T.T. Shen, H.Y. Zhu, Y.Q. Fu, S.T. Jiang, J.B. Li, J.L. Wang, Magnetic Fe3O4 embedded chitosan–crosslinked-polyacrylamide composites with enhanced removal of food dye: characterization, adsorption and mechanism, Int. J. Biol. Macromol. 227 (2023) 1234–1244, https://doi.org/10.1016/j.ijbiomac.2022.11.310.

[60] T.T.H. Le, K.S. Phan, B.T. Doan, T.T.T. Mai, H.B.H. Bui, H.N. Pham, T.D.T. Ung, Y. Wang, N.Q. Tran, L.H. Dang, P.T. Ha, Different conjugates of Fe3O4 nanoparticles, drug, and dye: optical and magnetic properties for in vivo bimodal imaging, RSC Adv. 15 (2025) 9644–9656, https://doi.org/10.1039/d4ra07910h.
[61] B. Zhang, X. Jiang, Magnetic nanoparticles mediated Thrombolysis-A review, IEEE Open Journal of Nanotechnology 4 (2023) 109–132, https://doi.org/10.1109/OJNANO.2023.3273921.
[62] X. Zhang, W. Cai, L. Hao, S. Feng, Q. Lin, W. Jiang, Preparation of Fe3O4/Reduced graphene oxide nanocomposites with good dispersibility for delivery of Paclitaxel, J. Nanomater. 2017 (1) (2017) 6702890, https://doi.org/10.1155/2017/6702890.
[63] D. Xia, F. Wang, S. Pan, S. Yuan, Y. Liu, Y. Xu, Redox/ph-responsive biodegradable thiol-hyaluronic acid/chitosan charge-reversal nanocarriers for triggered drug release, Polymers 13 (2021) 3785, https://doi.org/10.3390/polym13213785.
[64] F. Wang, N. Li, W. Wang, L. Ma, Y. Sun, H. Wang, J. Zhan, D. Yu, A multifunctional, highly biocompatible, and double-triggering caramelized nanotheranostic System loaded with Fe3O4 and DOX for combined chemo-photothermal therapy and real-time magnetic resonance imaging monitoring of triple negative breast cancer, Int. J. Nanomed. 18 (2023) 881–897, https://doi.org/10.2147/IJN.S393507.
[65] W. Yu, J. Koc, J.A. Finlay, J.L. Clarke, A.S. Clare, A. Rosenhahn, Layer-by-layer constructed hyaluronic acid/chitosan multilayers as antifouling and fouling-release coatings, Biointerphases 14 (2019) 051002, https://doi.org/10.1116/1.5110887.
[66] S. Shah, A. Chandra, A. Kaur, N. Sabnis, A. Lacko, Z. Gryczynski, R. Fudala, I. Gryczynski, Fluorescence properties of doxorubicin in PBS buffer and PVA films, J. Photochem. Photobiol., B 170 (2017) 65–69, https://doi.org/10.1016/j.jphotobiol.2017.03.024.
[67] E.S. Lisitsyna, A. Klose, E. Vuorimaa-Laukkanen, H. Ijäs, T. Lajunen, K. Suhling, V. Linko, T. Laaksonen, Fluorescence anisotropy for detailed analysis of doxorubicin loading into DNA origami nanocarriers for drug delivery, ACS Appl. Nano Mater. 8 (2025) 13274–13284, https://doi.org/10.1021/acsanm.5c01518.
[68] S. Shirazi-Fard, A.R. Zolghadr, A. Klein, How does aggregation of doxorubicin molecules affect its solvation and membrane penetration? New J. Chem. 47 (2023) 22063–22077, https://doi.org/10.1039/d2nj06221f.
[69] G.R. Mahdavinia, H. Hoseinzadeh, P. Labib, P. Jabbari, A. Mohebbi, S. Barzeger, H. Jafari, (Magnetic laponite/κ-carrageenan)@chitosan core–shell carrier for pH-sensitive release of doxorubicin, Polym. Bull 80 (2023) 12923–12943, https://doi.org/10.1007/s00289-023-04688-7.
[70] T. Wu, Y. He, L. Ding, F. Ding, F. Tan, Preparation and characterization of magnetic ferrite-chitosan nanoparticles delivery for DOX, Inorg. Chim. Acta. 559 (2024) 121791, https://doi.org/10.1016/j.ica.2023.121791.
[71] E. Kahraman, G. Nasun-Saygili, 5-Fluorouracil adsorption on graphene oxide-amine modified graphene oxide/hydroxyapatite composite for drug delivery applications: optimization and release kinetics studies, Heliyon 10 (19) (2024) e38494, https://doi.org/10.1016/j.heliyon.2024.e38494.
[72] I.R. Scolari, P.L. Páez, G.E. Granero, Synergistic bactericidal combinations between gentamicin and chitosan capped ZnO nanoparticles: a promising strategy for repositioning this first-line antibiotic, Heliyon 10 (2024) e25604, https://doi.org/10.1016/j.heliyon.2024.e25604.
[73] R.E. Schweppe, C. Korch, Challenges and advances in the development of cell lines and xenografts, Adv. Mol. Pathol. 1 (2018) 239–251, https://doi.org/10.1016/j.yamp.2018.07.004.
[74] H. Wei, Y. Hu, J. Wang, X. Gao, X. Qian, M. Tang, Superparamagnetic iron oxide nanoparticles: cytotoxicity, metabolism, and cellular behavior in biomedicine applications, Int. J. Nanomed. 16 (2021) 6097–6113, https://doi.org/10.2147/IJN.S321984.
[75] J. Liang, X. Yang, D. Liu, M. Cong, Y. Song, S. Bai, Lipid/Hyaluronic acid–coated Doxorubicin-Fe3O4 as a dual-targeting nanoparticle for enhanced cancer therapy, AAPS PharmSciTech 21 (2020), https://doi.org/10.1208/s12249-020-01764-3.
[76] J.S. Basuki, H.T.T. Duong, A. Macmillan, R.B. Erlich, L. Esser, M.C. Akerfeldt, R. M. Whan, M. Kavallaris, C. Boyer, T.P. Davis, Using fluorescence lifetime imaging microscopy to monitor theranostic nanoparticle uptake and intracellular doxorubicin release, ACS Nano 7 (2013) 10175–10189, https://doi.org/10.1021/nn404407g.
[77] J. Gautier, E. Munnier, M. Soucé, I. Chourpa, L. Douziech Eyrolles, Analysis of doxorubicin distribution in MCF-7 cells treated with drug-loaded nanoparticles by combination of two fluorescence-based techniques, confocal spectral imaging and capillary electrophoresis, Anal. Bioanal. Chem. 407 (2015) 3425–3435, https://doi.org/10.1007/s00216-015-8566-9.